Supplementary Information (SI) for Inorganic Chemistry Frontiers.


# Low-Valent Tantalum/Gold Clusters: Oxidation, Protonation, and C–H Activation

Michela L. Maiola and Joshua A. Buss*

Willard Henry Dow Laboratory, Department of Chemistry, University of Michigan 930 N. University Avenue, Ann Arbor, MI 48109 (USA)

## Supporting Information

## *Experimental Details*

### General Considerations

Unless otherwise specified, all operations were carried out in an MBraun drybox under a nitrogen atmosphere or using standard Schlenk and vacuum line techniques. All reaction glassware for air- and moisture-sensitive chemistry was dried at 140 °C for a minimum of 2 hours and cooled in either an evacuated glovebox antechamber or under vacuum on a Schlenk/vacuum line. Solvents for air- and moisture-sensitive reactions were dried over sodium benzophenone ketyl or by the method of Grubbs.[1] Deuterated solvents were purchased from Cambridge Isotope Laboratories and vacuum transferred from sodium benzophenone ketyl. Solvents, once dried and degassed, were vacuum transferred directly prior to use or stored under inert atmosphere over activated 4 Å molecular sieves (Fischer Scientific—activated under vacuum at 300 °C for 72 hours). $^{Et}$CAACAuCl,[2] [Na(THF)][Ta(naph)$_3$],[3] HBArF$_{24}$,[4] and FcBArF$_{24}$[5] were prepared according to literature procedures. Commercial reagents were purchased from standard vendors and used without further purification unless noted otherwise.

Electrochemical experiments were carried out with a CH Instruments CH630E potentiostat. A standard three-electrode cell, employing a silver wire pseudo-reference, platinum wire counter, and glassy carbon working electrode, was utilized for all measurements. Cyclic voltammetry experiments were performed in 0.1 M [$^n$Bu$_4$N][BArF$_{24}$] dimethoxyethane (DME) solution. The samples were internally referenced to $Fc^{0/+}$ (sublimed under reduced pressure).

IR spectra were recorded on a Nicolet Summit PRO FTIR Spectrometer equipped with an ATR attachment featuring an AR-Coated Diamond. The spectrometer is housed in an MBraun drybox under a nitrogen atmosphere. Samples were either drop cast or deposited as solids on the crystal plate.

$^{1}H$ and $^{13}C\{^{1}H\}$ spectra were recorded on a Bruker Avance Neo 500 MHz (Prodigy BBO Cryoprobe), Varian Vnmrs 700 MHz (PFG AutoX Broadband Probe), Varian Vnmrs 600 MHz (PFF AutoX Dual Broadband probe), Varian Vnmrs 400 MHz (Autoswitchable probe), or Varian Vnmrs 400 MHz (PFG AutoX Dual Broadband probe) spectrometer with shifts reported in parts per million (ppm). $^{2}H$ spectra were recorded on a Varian Vnmrs 700 MHz (PFG AutoX Broadband Probe) spectrometer with shifts reported in parts per million (ppm). $^{1}H$, $^{2}H$, and $^{13}C\{^{1}H\}$ spectra are referenced to residual solvent peaks.[6] Multiplicities are abbreviated as follows: s = singlet, d = doublet, t = triplet, q = quartet, sept = septet, dd = doublet of doublets, dt = doublet of triplets, td = triplet of doublets, qq = quartet of quartets, vt = virtual triplet, d vt = doublet of virtual triplets, m = multiplet, br = broad, and v br = very broad (multiplicity assignments are omitted for “v br” assignments due to poor resolution). Diisopropyl phenyl (dipp) ring positions are labeled as outlined below:

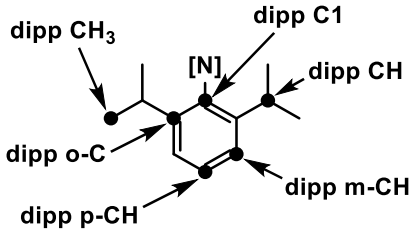


The bulk purity of most diamagnetic complexes was established via qNMR[7] rather than combustion analysis.[8] Previous work in our lab has shown that this technique correlates with combustion analysis results for related multinuclear clusters.[9] In each qNMR assay, a hexamethyldisiloxane (HMDSO) standard was added to a $C_6D_6$ solution of each analyte unless otherwise specified. $^{1}H$ NMR spectra (1 scan) was collected with a 90° pulse angle. The relative peak integration of the standard ($\delta_{HMDSO}$ = 0.12 ppm) and that of each baseline-resolved compound ligand proton signal was recorded; these values were used to determine the percent purity employing the formula below (n = number of protons giving rise to the integral, Int = integral value, MW = molecular weight, m = exact weight of sample, ic = internal standard, t = target analyte). The values reported for each compound represent an average of the percent purity as determined for each ligand proton signal.

$$P\ [\%] = \frac{n_{ic} * Int_t * MW_t * m_{ic}}{n_t * Int_{ic} * MW_{ic} * m_t}$$

## Synthesis of 1 and 2

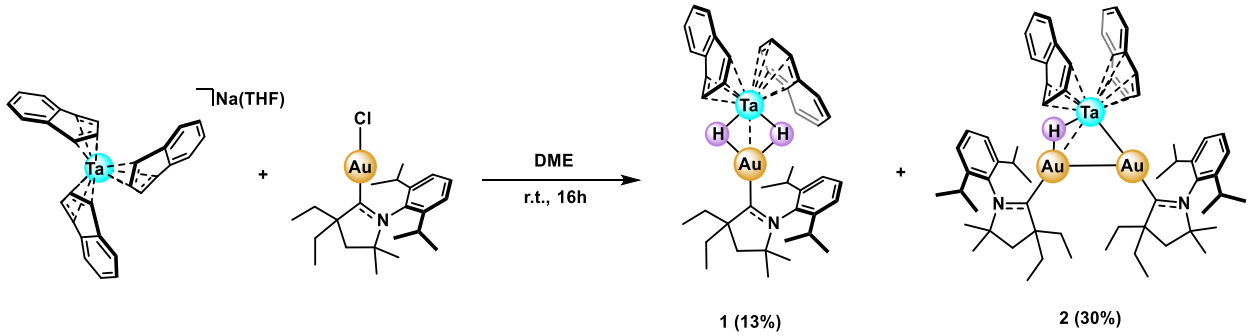


A 100 mL round bottom flask was charged with a DME (30 mL) solution of $^{Et}$CAACAuCl (506.6 mg, 0.93 mmol) and a stir bar. A suspension of $[Ta(C_{10}H_8)_3]^-$ (613.0 mg, 0.93 mmol) in DME (20 mL) was added dropwise, with stirring. The reaction mixture was left to stir at room temperature for 16 hours, affording a deep red solution. At this time, volatiles were removed *in vacuo* and the resulting residue was triturated with hexanes (20 mL). The solids were extracted into hexanes and filtered through a sintered glass frit packed with a bed of Celite until it ran clear (~50 mL). The remaining solids on the round bottom flask and Celite pad were extracted into diethyl ether until the filtrate ran clear (~100 mL). The dark red diethyl ether filtrate was dried *en vacuo*. The resulting dark red solids were extracted into hexanes until the washes ran clear (~30 mL), and the red filtrate was combined with the previous hexanes filtrate and volatiles were removed, affording **1** as red/brown solids (114.8 mg, 0.120 mmol, 13%) The remaining solids on the round bottom flask and Celite pad were extracted into THF (50 mL), then dried *en vacuo*. These brown solids were extracted into diethyl ether (50 mL) and the red filtrate was dried *en vacuo*, affording **2** as dark red solids (204.0 mg, 0.140 mmol, 30%). X-ray quality crystals of **2** were grown via vapor diffusion of pentane into a toluene solution of $(^{Et}CAACAu)_2TaH(C_{10}H_8)_2$ at −35 °C. Note: Various Ta:Au stoichiometries were tested and the reaction showed optimal yield of **2** with a metal ratio of 1:1. Based on detailed isotopic labeling studies on our related Ta/Cu system,[9b] the hydride ligands are likely sourced from naphthalene and solvent; however, H/D scrambling inhibited definitive isotopic labeling studies in the present system.

$^1$H (500 MHz, THF-$d_8$, 25 °C) δ (ppm): 7.43 (t, $J$ = 7.7 Hz, 2H, dipp p-C*H*), 7.34 (d, $J$ = 7.7 Hz, 4H, dipp m-C*H*), 5.83 (m, 8H, naphthyl-C*H*), 4.79 (s, 4H, naphthyl-C*H*), 3.12 (s, 4H, naphthyl-C*H*), 2.97 (sept, $J$ = 6.9 Hz, 4H, dipp C*H*), 1.97 (s, 4H, carbene-C$H_2$), 1.95-1.75 (m, 8H, ethyl-C$H_2$), 1.67 (d, $J$ = 6.5 Hz, 12H, dipp C$H_3$), 1.41 (s, 12H, carbene-C$H_3$), 1.29 (d, $J$ = 6.6 Hz, 12H, dipp C$H_3$), 1.01 (m, 12H, ethyl-C$H_3$), –1.79 (s, 1H, hydride).

$^{13}$C{$^1$H} (126 MHz, THF-$d_8$, 25 °C) δ (ppm): 145.96 (s, dipp o-*C*), 136.99 (s, dipp *C*1), 129.72 (s, dipp p-*C*H), 128.76 (s, benzene impurity), 125.65 (s, dipp m-*C*H), 125.08 (s, naphthyl-*C*H), 123.50 (s, naphthyl-*C*H), 91.69 (s, naphthyl-*C*H), 80.42 (s, carbene-*C*$(CH_3)_2$), 63.81 (s, carbene-*C*$(CH_2CH_3)_2$), 42.57 (s, carbene-*C*$H_2$), 34.86 (s, hexanes impurity), 31.25 (s, ethyl-*C*$H_2$), 30.46 (s, H-grease impurity), 29.75 (s, carbene-*C*$H_3$), 29.52 (s, dipp *C*H), 27.16 (s, dipp *C*$H_3$), 24.00 (s, dipp *C*$H_3$), 23.01 (s, hexanes impurity),

14.18 (s, hexanes impurity), 9.37 (s, ethyl-$CH_3$). Note: The CAAC carbene carbon and two of the napthyl carbons were not discernable in either the 1D or 2D data, likely due to the dynamicity of the complex.

qNMR ($^1$H NMR, 400MHz, $C_6D_6$ with HMDSO standard, 25 °C): 96%

Note: Given the demonstrated photochemical activation of related heterometallic hydride complexes,[10] we investigated the role of light in the salt metathesis chemistry. When running the salt metathesis reaction in the dark, complex **2** is still formed as the major product (29% yield), but there is only a small amount of **1** formed in addition to a host of soluble byproducts, suggesting light may be involved in the formation of **1** under the standard salt metathesis conditions.

**Synthesis of 1 from 2**

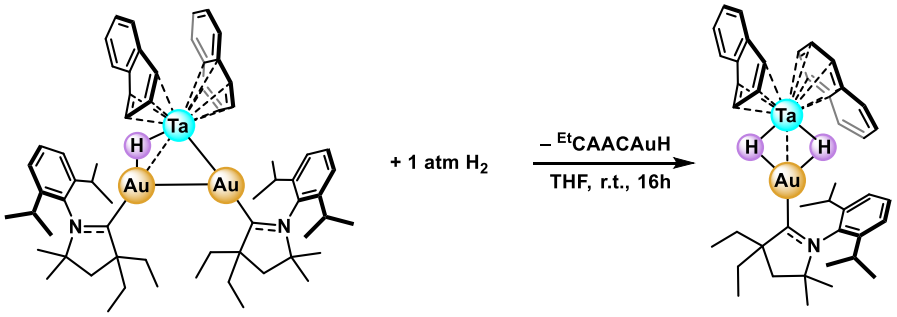


2 1 (69%)

A Teflon-stoppered Schlenk tube was charged with a deep red THF (40 mL) solution of ($^{Et}$CAACAu)$_2$TaH($C_{10}H_8$)$_2$ (263.7 mg, 0.18 mmol) and a stir bar. The tube was sealed, degassed via three freeze-pump-thaw cycles, and backfilled with $H_2$ (1 atm). The reaction was stirred for 16 hours at room temperature, during which time the color changed from deep red to orange. The solvent was removed *in vacuo*. The resultant solids were triturated with hexanes (2 x 10 mL), extracted into diethyl ether (40 mL), and filtered through Celite. The filtrate was dried under reduced pressure, affording ($^{Et}$CAACAu)TaH$_2$($C_{10}H_8$)$_2$ (**1**) as an orange solid (125.0 mg, 0.125 mmol, 69.1%). X-ray quality crystals were grown via vapor diffusion of pentane into a THF solution of ($^{Et}$CAACAu)TaH$_2$($C_{10}H_8$)$_2$ at −35 °C.

$^1$H (500 MHz, $C_6D_6$, 25 °C) δ (ppm): 7.19 (m, 1H, dipp p-C*H*), 7.01 (d, *J* = 7.6 Hz, 2H, dipp m-C*H*), 6.43 (m, 8H, naphthyl-C*H*), 5.24 (s, 4H, naphthyl-C*H*), 4.33 (s, 4H, naphthyl-C*H*), 2.73 (m, 2H, isopropyl-C*H*), 1.63 (m, 2H, ethyl-C$H_2$), 1.54 (d, *J* = 6.8 Hz, 6H, dipp C$H_3$), 1.43 (s, 2H, carbene-C$H_2$), 1.38 (m, 2H, ethyl-C$H_2$), 1.08 (d, *J* = 6.7 Hz, 6H, dipp C$H_3$), 0.93-0.79 (m, 12H, overlapping carbene-C$H_3$ and two ethyl-C$H_3$*'s*), –2.78 (s, 2H, hydrides).

$^{13}$C{$^1$H} (126 MHz, $C_6D_6$, 25 °C) δ (ppm): 253.96 (s, carbene-*C*), 147.40 (s, naphthyl-$C_{bridge}$), 145.82 (s, naphthyl-$C_{bridge}$), 145.69 (s, dipp o-*C*), 145.37 (s, naphthyl-$C_{bridge}$), 136.19 (s, dipp-*C*1), 132.48 (s, naphthyl-$C_{bridge}$), 129.82 (s, dipp p-*C*H), 126.52 (s, naphthyl-CH), 125.52 (s, naphthyl-*C*H), 125.44 (s, dipp m-*C*H), 95.76 (s, naphthyl-*C*H),

78.57 (s, carbene-*C*($C_2H_5$)$_2$), 68.08 (s, naphthyl-*C*H), 61.08 (s, carbene-*C*($CH_3$)$_2$), 43.52 (s, carbene-*C*$H_2$), 31.85 (s, ethyl-*C*$H_2$), 29.24 (s, dipp *C*H), 28.88 (s, carbene-*C*$H_3$), 26.11 (s, dipp *C*$H_3$), 23.85 (s, dipp *C*$H_3$), 9.14 (s, ethyl-*C*$H_3$).

qNMR ($^1$H NMR, 400MHz, $C_6D_6$ with HMDSO standard, 25 °C): 94%

**Synthesis of 3**

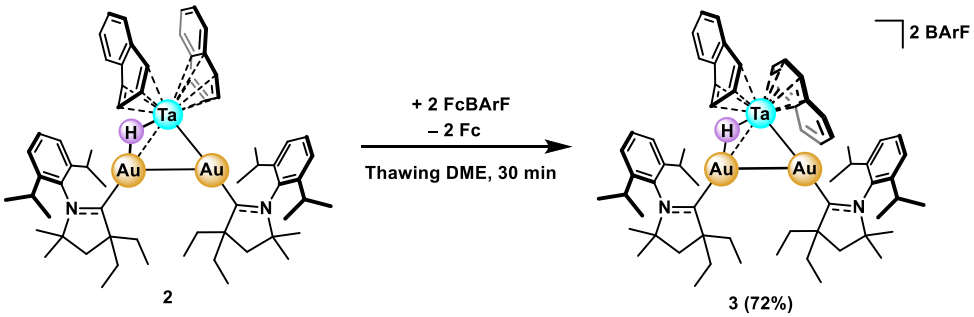


A 20 mL scintillation vial was charged with a DME (3 mL) solution of ($^{Et}$CAACAu)$_2$TaH($C_{10}H_8$)$_2$ (21.6 mg, 0.0148 mmol) and a stir bar. A second scintillation vial was charged with a DME (2 mL) solution of FcBArF (31.1 mg, 0.0296 mmol). Both vials were placed in a liquid nitrogen ($LN_2$) chilled cold well and the contents frozen. The FcBArF solution was removed from the cold well, and upon thawing, was added dropwise to the thawing ($^{Et}$CAACAu)$_2$TaH($C_{10}H_8$)$_2$ solution, with stirring. Stirring continued at room temperature for 30 minutes, affording a light orange solution. The reaction mixture was dried *in vacuo* and the resulting residue was triturated with pentane (2 x 5 mL). The solids were washed with hexanes (8 mL), extracted into benzene (8 mL), and filtered over a bed of Celite. The light orange filtrate was lyophilized under reduced pressure, affording crude [($^{Et}$CAACAu)$_2$TaH($C_{10}H_8$)$_2$][BArF]$_2$ (**3**) as a light orange powder (33.8 mg, 0.011 mmol, 71.7%).

$^1$H (500 MHz, DME-$d_{10}$, 25 °C) δ (ppm): 7.69 (s, 16H, BArF o-C*H*), 7.56 (s, 8H, BArF p-C*H*), 7.49 (t, *J* = 7.8 Hz, 2H, dipp p-C*H*), 7.34 (d, *J* = 7.8 Hz, 4H, dipp m-C*H*), 7.27 (m, 2H, naphthyl-C*H*), 7.18 (m, 2H, naphthyl-C*H*), 6.67 (m, 2H, naphthyl-C*H*), 6.56 (m, 2H, naphthyl-C*H*), 6.43 (m, 2H, naphthyl-C*H*), 5.23 (t, *J* = 3.8 Hz, 2H, naphthyl-C*H*), 4.12 (m, 2H, naphthyl-C*H*), 4.03 (s, 5H, impurity), 3.50 (m, 2H, impurity), 3.27 (s, 10H, impurity), 3.25 (m, 2H, naphthyl-C*H*), 2.79 (sept, *J* = 6.8 Hz, 4H, dipp C*H*), 2.27 (m, 2H, impurity), 2.14 (s, 4H, carbene-C$H_2$), 1.80 (m, 4H, ethyl-C$H_2$), 1.67 (m, 4H, ethyl-C$H_2$), 1.45 (s, 1H, hydride), 1.40 (s, 12H, carbene-C$H_3$), 1.30 (d, *J* = 6.7 Hz, 12H, dipp C$H_3$), 1.26 (d, *J* = 6.7 Hz, 12H, dipp C$H_3$), 1.04 (t, *J* = 7.4 Hz, 12H, ethyl-C$H_3$).

$^{13}$C{$^1$H} (126 MHz, DME-$d_{10}$, 25 °C) δ (ppm): 248.69 (s, carbene-*C*), 161.91 (q, *J* = 49.9 Hz, BArF B-*C*), 145.23 (s, dipp o-*C*), 143.53 (s, naphthyl-*C*$_{bridge}$), 134.93 (s, BArF o-*C*H), 134.01 (s, dipp *C*1), 132.72 (s, naphthyl-*C*H), 130.83 (s, dipp p-*C*H), 129.62 (s, naphthyl-*C*H), 129.41 (q, *J* = 31.8 Hz, BArF m-*C*), 125.36 (s, dipp m-*C*H), 124.83 (q, *J* = 271.95 Hz, BArF *C*$F_3$), 123.27 (s, naphthyl-*C*H), 121.00 (s, naphthyl-*C*$_{bridge}$), 120.53 (s, naphthyl-

*C*H), 117.61 (s, BArF p-*C*H), 117.00 (s, naphthyl-*C*H), 108.61 (s, naphthyl-*C*H), 89.64 (s, naphthyl-*C*H), 82.76 (s, carbene-*C*$(CH_3)_2$), 72.75 (s, impurity), 71.59 (s, naphtyl-*C*H), 67.93 (s, impurity), 62.80 (s, carbene-*C*$(C_2H_5)_2$), 58.15 (s, impurity), 41.71 (s, carbene-*C*$H_2$), 31.52 (s, ethyl-*C*$H_2$), 29.43 (s, dipp *C*H), 28.70 (s, carbene-*C*$H_3$), 27.13 (s, dipp *C*$H_3$), 22.04 (s, dipp *C*$H_3$), 9.17 (s, ethyl-*C*$H_3$).

qNMR ($^1$H NMR, 400MHz, DME-$d_{10}$ with HMDSO standard, 25 °C): 91%

**Synthesis of 4**

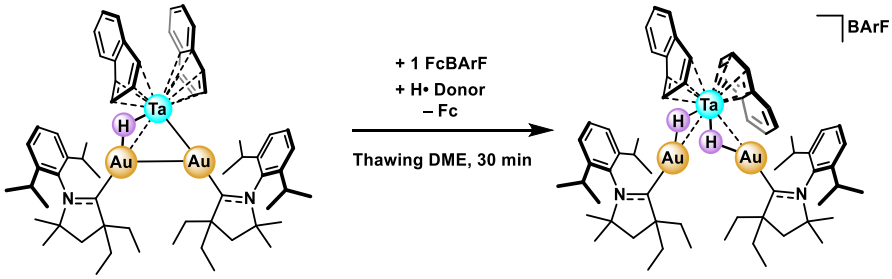


A 20 mL scintillation vial was charged with a DME (3 mL) solution of ($^{Et}$CAACAu)$_2$TaH($C_{10}H_8$)$_2$ (23.6 mg, 0.0162 mmol) and a stir bar. A second scintillation vial was charged with a DME (2 mL) solution of FcBArF (17.0 mg, 0.0162 mmol). Both vials were placed in a liquid nitrogen ($LN_2$) chilled cold well and the contents frozen. The FcBArF solution was removed from the cold well, and upon thawing, was added dropwise to the thawing ($^{Et}$CAACAu)$_2$TaH($C_{10}H_8$)$_2$ solution, with stirring. Stirring continued at room temperature for 30 minutes, affording a red-brown solution. The reaction mixture was dried *in vacuo* and the resulting residue was triturated with pentane (2 x 5 mL). The solids were washed with benzene (10 mL), extracted into diethyl ether (8 mL), and filtered over a bed of Celite. The red-brown ether filtrate was dried under reduced pressure, affording [($^{Et}$CAACAu)$_2$TaH($C_{10}H_8$)$_2$][BArF] (**4**) as a brown solid (13.7 mg, 0.006 mmol, 36.0%). Note: **4** is thermally unstable and decomposes as a solid at room temperature over 8 days, and in solution at room temperature over 3 hours. However, **4** proves stable at −35 °C both in solution and in the solid state. X-ray quality crystals were grown via vapor diffusion of pentane into a saturated THF solution of [($^{Et}$CAACAu)$_2$TaH$_2$($C_{10}H_8$)$_2$][BArF] at −35 °C.

$^1$H (700 MHz, THF-$d_8$, −35 °C) δ (ppm): 7.85 (s, 8H, BArF o-C*H*), 7.69-7.66 (m, 2H, overlapping dipp p-C*H* and dipp m-C*H*), 7.64 (s, 4H, BArF p-C*H*), 7.63-7.61 (m, 1H, dipp p-C*H*), 7.54-7.45 (m, 2H, overlapping dipp m-C*H*), 7.41 (d, *J* = 7.8 Hz, dipp m-C*H*), 7.37 (d, *J* = 7.7 Hz, 1H, naphthyl-C*H*), 7.33 (benzene impurity), 6.80 (t, *J* = 7.5 Hz, 1H, naphthyl-C*H*), 6.73 (t, *J* = 7.3 Hz, 1H, naphthyl-C*H*), 6.65 (t, *J* = 7.4 Hz, 1H, naphthyl-C*H*), 6.50 (d, *J* = 8.5 Hz, 1H, naphthyl-C*H*), 6.38 (m, 3H, overlapping naphthyl-C*H*), 6.31 (d, *J* = 7.4 Hz, 1H naphthyl-C*H*), 5.48 (m, 1H, naphthyl-C*H*), 5.33 (t, *J* = 7.1 Hz, 2H, naphthyl-C*H*), 4.21 (d, *J* = 7.6 Hz, 1H, naphthyl-C*H*), 3.75 (d, *J* = 6.9 Hz, 1H, naphthyl-C*H*), 3.48 (t, *J* = 6.8 Hz, 1H, naphthyl-C*H*), 3.25 (d, *J* = 6.9 Hz, 1H, naphthyl-C*H*), 3.19 (impurity), 2.94 (m, 2H, dipp C*H*), 2.81 (sept, *J* = 6.7 Hz, 1H, dipp C*H*), 2.67 (sept, *J* = 6.8 Hz, 1H,

dipp C*H*), 2.28 (s, 2H, carbene-C$H_2$), 2.18 (s, 1H, carbene-C$H_2$), 2.10-1.76 (m, 9H, overlapping carbene-C$H_2$ and ethyl-C$H_2$), 1.70 (impurity), 1.65 (s, 3H, carbene-C$H_3$), 1.61 (s, 6H, carbene-C$H_3$), 1.49-1.41 (m, 12H, overlapping carbene-C$H_3$ and impurity), 1.36 (d, *J* = 6.6 Hz, 3H, dipp C$H_3$), 1.34 (d, *J* = 6.4 Hz, 3H, dipp C$H_3$), 1.31 (d, *J* = 6.4 Hz, 6H, dipp C$H_3$), 1.28 (d, *J* = 6.8 Hz, dipp C$H_3$), 1.24-1.17 (m, 6H, overlapping dipp C$H_3$ and ethyl-C$H_3$), 1.11 (t, *J* = 7.4 Hz, 3H, ethyl-C$H_3$), 1.09-1.02 (m, 6H, overlapping dipp C$H_3$ and ethyl-C$H_3$), 0.89 (m, 6H, overlapping dipp C$H_3$ and impurity), 0.78 (t, *J* = 7.4 Hz, 3H, ethyl-C$H_3$), −4.26 (s, 1H, hydride), −5.27 (s, 1H, hydride).

$^{13}$C (176 MHz, THF-$d_8$, −35 °C) δ (ppm): 252.58 (s), 247.99 (s), 162.67 (q), 145.64 (q), 144.88 (s), 137.18 (s), 135.65 (s), 135.26 (s), 134.35 (s), 131.98 (s), 131.46 (s), 131.06 (s), 130.69 (s), 129.75 (q), 128.91 (s), 128.78 (s), 128.44 (s), 127.57 (s),126.72 (s), 126.42 (s), 126.02 (s), 125.82 (s), 124.47 (s), 124.03 (s), 123.19 (s), 122.92 (s), 120.94 (s), 120.58 (s), 118.10 (s), 115.72 (s), 115.60 (s), 111.89 (s), 101.41 (s), 100.69 (s), 96.43 (s), 94.28 (s), 84.20 (s), 83.27 (s), 82.83 (s), 75.63 (s), 68.21 (s), 63.60 (s), 63.19 (s), 63.11 (s), 62.64 (s), 41.14 (s), 40.36 (s), 40.01 (s), 35.02 (s), 33.02 (s), 31.82 (t), 30.88 (s), 30.21 (s), 29.92 (s), 29.80 (s), 29.63 (s), 29.49 (s), 29.29 (s), 28.83 (s), 27.61 (s), 27.41 (s), 26.66 (s), 23.97 (s), 23.79 (s), 23.30 (s), 23.25 (s), 22.80 (s), 22.42 (s), 14.45 (s), 10.32 (s), 10.16 (s), 9.68 (s), 8.99 (s), 8.92 (s).

Note: The instability of **4** leads to impurities in the NMR spectra that prohibit a definitive assignment for each $^{13}$C signal, even with the aid of the 2D data. The decomposition of the product is further reflected in the bulk purity, as determined by qNMR.

qNMR ($^1$H NMR, 700MHz, THF-$d_8$ with HMDSO standard, −35 °C): 69%

## Independent Synthesis of 4

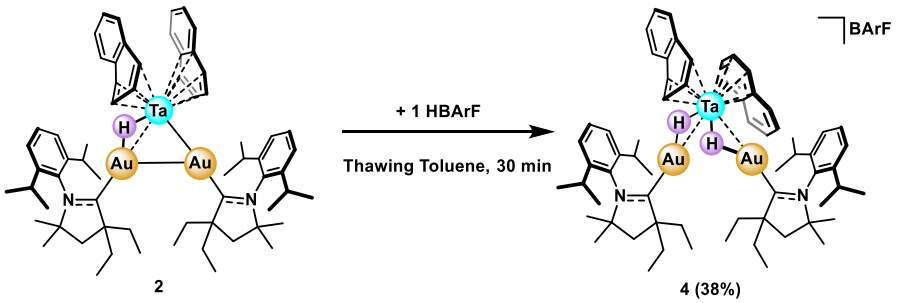


To corroborate the structural assignment of **4**, an independent synthesis was pursued. A 20 mL scintillation vial was charged with a toluene (4 mL) solution of ($^{Et}$CAACAu)$_2$TaH(C$_{10}$H$_8$)$_2$ (42.9 mg, 0.0294 mmol) and a stir bar. A second scintillation vial was charged with a toluene (3 mL) solution of HBArF (23.0 mg, 0.0227 mmol). Both vials were placed in a liquid nitrogen ($LN_2$) chilled cold well and the contents frozen. The HBArF solution was removed from the cold well, and upon thawing, was added dropwise to the thawing ($^{Et}$CAACAu)$_2$TaH(C$_{10}$H$_8$)$_2$ solution, with stirring. Minimal ether (~0.2 mL) was used

to wash the remaining HBArF residue into the reaction vial. Stirring continued at room temperature for 30 minutes, affording a dark orange oil suspended in a dark orange solution. The reaction mixture was dried *in vacuo* and the resulting residue was triturated with pentane (2 x 5 mL). The solids were washed with benzene (10 mL), extracted into ether (8 mL), and filtered over a bed of Celite. The orange-brown filtrate was dried under reduced pressure, affording [($^{Et}$CAACAu)$_2$TaH$_2$(C$_{10}$H$_8$)$_2$][BArF] (**4**) as a brown solid (39.3 mg, 0.017 mmol, 38.0%). Note: The separation of **4** from [($^{Et}$CAACAu)$_2$H][BArF] byproducts was unsuccessful.

**Synthesis of 5**

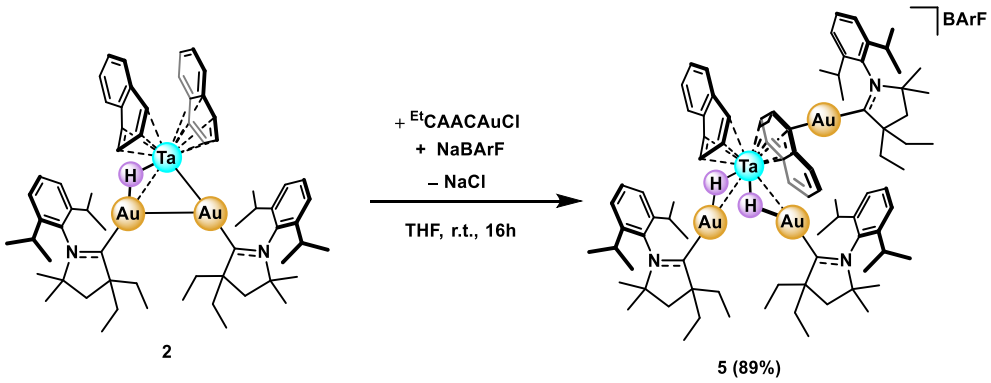


A 20 mL scintillation vial was charged with a THF (4 mL) solution of ($^{Et}$CAACAu)$_2$TaH(C$_{10}$H$_8$)$_2$ (23.5 mg, 0.0161 mmol) and a stir bar. A THF (2 mL) solution of CAACAuCl (8.8 mg, 0.0161 mmol) was added dropwise, with stirring. Subsequently, a THF (2 mL) solution of NaBArF (14.3 mg, 0.016 mmol) was added to the reaction mixture dropwise, with stirring. Stirring continued at room temperature for 16 hours, affording a dark red solution. The reaction mixture was dried *in vacuo* and the resulting residue was triturated with pentane (2 x 5 mL). The solids were washed with diethyl ether (8 mL), extracted into benzene (10 mL), and filtered over a bed of Celite. The dark red filtrate was dried under reduced pressure, affording [($^{Et}$CAACAu)$_3$TaH$_2$(C$_{10}$H$_8$)(C$_{10}$H$_7$)][BArF], (**5**) as a red solid (40.3 mg, 0.014 mmol, 89%). X-ray quality crystals were grown via layering of pentane onto a saturated toluene solution of [($^{Et}$CAACAu)$_3$TaH$_2$(C$_{10}$H$_8$)(C$_{10}$H$_7$)][BArF] at 25 °C.

$^1$H (500 MHz, C$_6$D$_6$, 25 °C) δ (ppm): 8.43 (s, 8H, BArF o-C*H*), 7.74 (s, 4H, BArF p-C*H*), 7.24 (m, 3H, overlapping dipp m-C*H* and dipp p-C*H*), 7.14-6.95 (m, 6*H*, overlapping dipp m-C*H* and dipp p-C*H*), 6.94 (d, *J* = 5.3 Hz, 1H, naphthyl-C*H*), 6.74 (dd, *J* = 5.2, 3.1 Hz, 2H, naphthyl-C*H*), 6.64 (t, *J* = 7.6 Hz, 1H, naphthyl-C*H*), 6.53 (t, *J* = 7.5 Hz, 1H, naphthyl-C*H*), 6.23 (dd, *J* = 5.3, 3.2 Hz, 1H, naphthyl-C*H*), 6.05 (dd, *J* = 5.3, 3.2 Hz, 1H, naphthyl-C*H*), 5.98 (t, *J* = 6.5 Hz, 2H, naphthyl-C*H*), 5.89 (m, 1H, naphthyl-C*H*), 5.64 (m, 1H, naphthyl-C*H*), 3.86 (d, *J* = 7.1 Hz, 1H, naphthyl-C*H*), 3.58 (THF impurity), 3.49 (t, *J* = 6.6 Hz, 1H, naphthyl-C*H*), 2.87-2.46 (m, 8H, overlapping naphthyl-C*H* and dipp C*H*), 2.05 (m, 1H, ethyl-C*H*$_2$), 1.84 (m, 1H, ethyl-C*H*$_2$), 1.79-1.53 (m, 10H, overlapping carbene C*H*$_2$ and

ethyl-C*H*$_2$), 1.49 (d, *J* = 3.5 Hz, 3H, dipp C*H*$_3$), 1.45 (d, *J* = 6.7 Hz, 3H, dipp C*H*$_3$), 1.35 (m, 6H, overlapping dipp C*H*$_3$), 1.30-1.18 (m, 12H, overlapping carbene-C*H*$_3$), 1.18-1.10 (m, 9H, overlapping dipp C*H*$_3$ and carbene-C*H*$_3$), 1.08 (d, *J* = 6.7 Hz, 3H, dipp C*H*$_3$), 1.05-0.94 (m, 15H, overlapping dipp C*H*$_3$), 0.94-0.64 (m, 18H, overlapping ethyl-C*H*$_3$), −3.16 (s, 1H, hydride), −5.89 (s, 1H, hydride).

$^{13}$C{$^1$H} (126 MHz, $C_6D_6$, 25 °C) δ (ppm): 256.71 (s, carbene-*C*), 256.63 (s, carbene-*C*), 248.45 (s, carbene-*C*), 162.82 (q, *J* = 49.62 Hz, BArF B-*C*), 145.92 (q, J = 59.13 Hz, BArF m-*C*), 145.16 (s, dipp o-*C*), 145.08 (s, dipp o-*C*), 144.96 (s, dipp o-*C*), 136.46 (s, naphthyl-*C*$_{bridge}$), 130.60 (s, dipp m-*C*H), 130.48 (s, naphthyl-*C*H), 130.20 (s, naphthyl-*C*$_{bridge}$), 130.04 (s, dipp p-*C*H), 129.79 (s, dipp p-*C*H), 127.34 (s, naphthyl-*C*H), 126.45 (s, naphthyl-*C*H), 125.88 (s, naphthyl-*C*-Au), 125.18 (q, *J* = 270.49, BArF *C*F$_3$), 125.12 (s, dipp p-*C*H), 124.91 (s, dipp m-*C*H), 124.81 (s, naphthyl-*C*H), 122.12 (s, naphthyl-*C*H), 121.68 (s, naphthyl-*C*H), 120.83 (s, naphthyl-*C*H),119.79 (s, naphthyl-*C*H), 118.10 (s, BArF p-*C*H), 116.66 (naphthyl-*C*$_{bridge}$), 115.55 (s, naphthyl-*C*H), 102.92 (s, naphthyl-*C*H), 97.98 (s, naphthyl-*C*H), 93.02 (s, naphthyl-*C*H), 81.82 (s, dipp *C*1), 81.44 (s, dipp *C*1), 80.33 (s, dipp *C*1), 76.60 (s, naphthyl-*C*H), 69.70 (s, naphthyl-*C*H), 67.83 (THF impurity), 63.63 (s, carbene-*C*($C_2H_5$)$_2$), 63.23 (s, naphthyl-*C*H), 62.79 (s, carbene-*C*($C_2H_5$)$_2$), 41.81 (s, carbene-*C*H$_2$), 40.62 (s, carbene-*C*H$_2$), 40.24 (s, carbene-*C*H$_2$), 32.76 (s, ethyl-*C*H$_2$), 31.99 (s, ethyl-*C*H$_2$), 31.88 (s, ethyl-*C*H$_2$), 31.63 (s, ethyl-*C*H$_2$), 31.53 (s, ethyl-*C*H$_2$), 31.45 (s, ethyl-*C*H$_2$), 29.54 (s, dipp *C*H), 29.35 (s, dipp *C*H), 28.91 (s, dipp *C*H), 28.76 (s, dipp *C*H), 28.66 (s, carbene-*C*($CH_3$)$_2$), 28.46 (s, carbene-*C*($CH_3$)$_2$), 27.67 (s, dipp *C*H$_3$), 27.60 (s, dipp *C*H$_3$), 27.40 (s, dipp *C*H$_3$), 27.16 (s, dipp *C*H$_3$), 26.51 (s, dipp *C*H$_3$), 26.34 (s, dipp *C*H$_3$), 23.90 (s, carbene-*C*H$_3$), 23.31 (s, carbene-*C*H$_3$), 22.96 (s, carbene-*C*H$_3$), 22.44 (s, carbene-*C*H$_3$), 22.20 (s, carbene-*C*H$_3$), 10.09 (s, ethyl-*C*H$_3$), 9.88 (s, ethyl-*C*H$_3$),9.63 (s, ethyl-*C*H$_3$), 9.44 (s, ethyl-*C*H$_3$), 9.40 (s, ethyl-*C*H$_3$), 9.28 (s, ethyl-*C*H$_3$).

qNMR ($^1$H NMR, 400MHz, $C_6D_6$ with HMDSO standard, 25 °C): 88%

## *NMR Spectra*

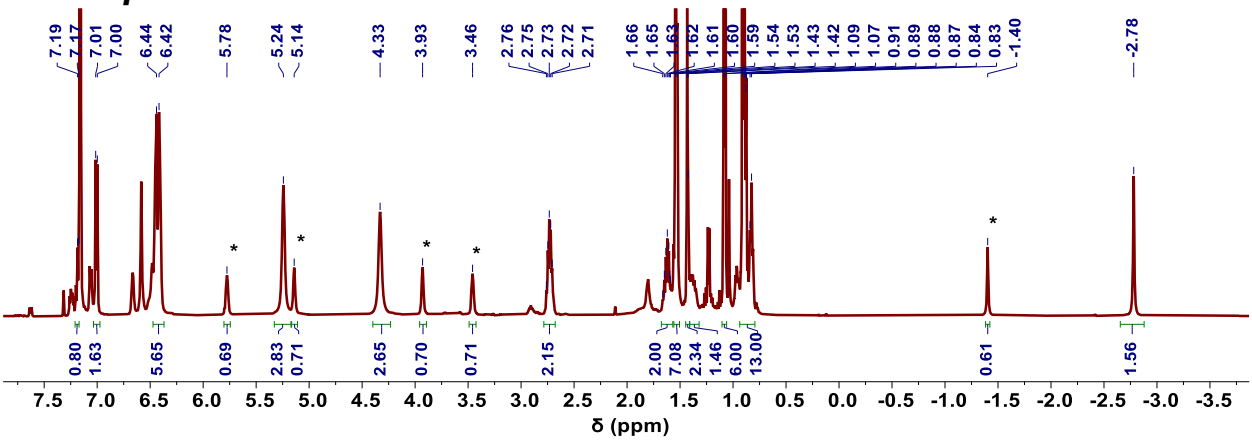


**Figure S1** – $^{1}$H NMR Spectrum of **1** (500 MHz, $C_6D_6$, 25 °C). Signals corresponding to the minor (anti) conformation are designated with an asterisk. Note: Naphthyl-C*H* peaks of the major species integrate low, relative to the ligand peaks, due to the dynamic naphthyl ring slip.

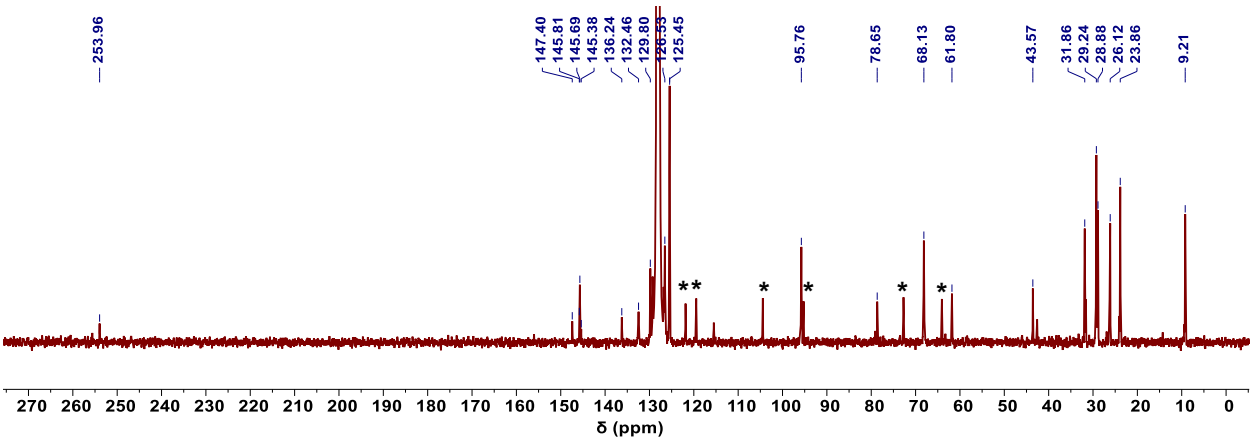


**Figure S2** – $^{13}C\{^{1}H\}$ NMR Spectrum of **1** (126 MHz, $C_6D_6$, 25 °C). Signals corresponding to the minor (anti) conformation are designated with an asterisk.

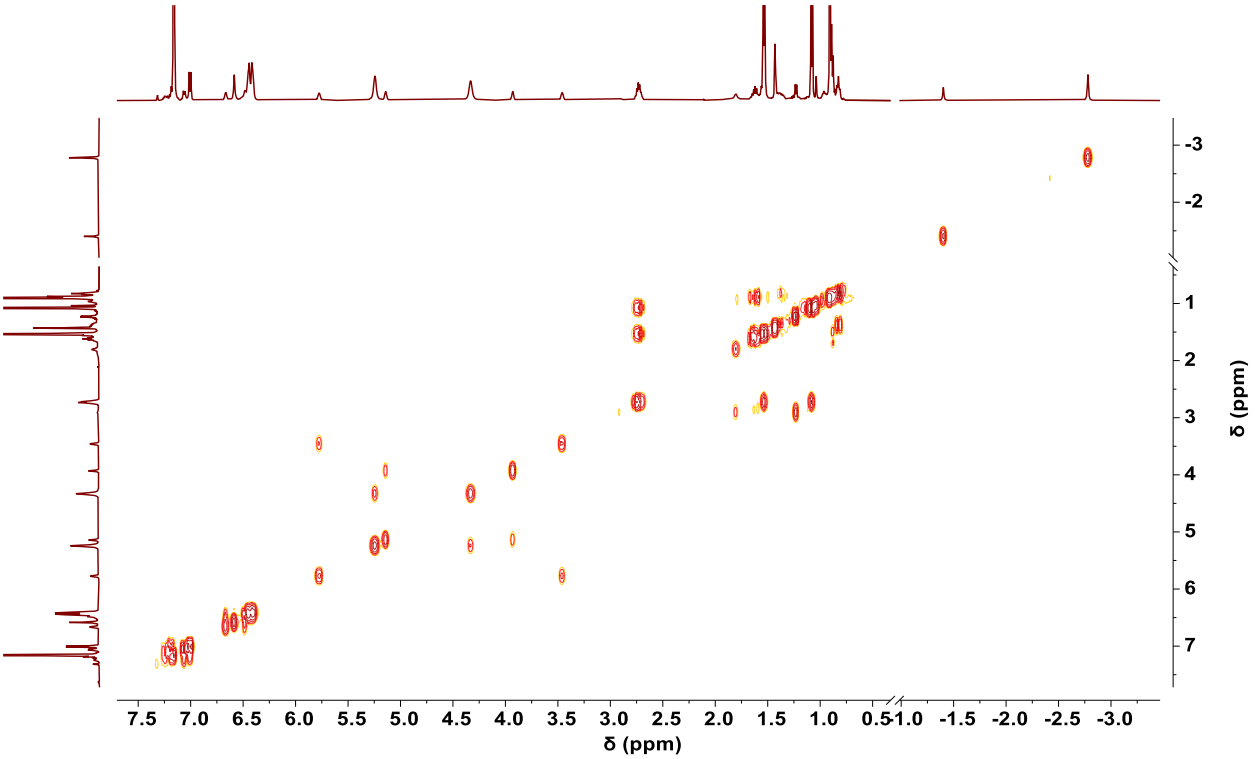


**Figure S3** – Partial $^{1}H/^{1}H$ COSY NMR Spectrum of **1** (500 MHz, $C_6D_6$, 25 °C).

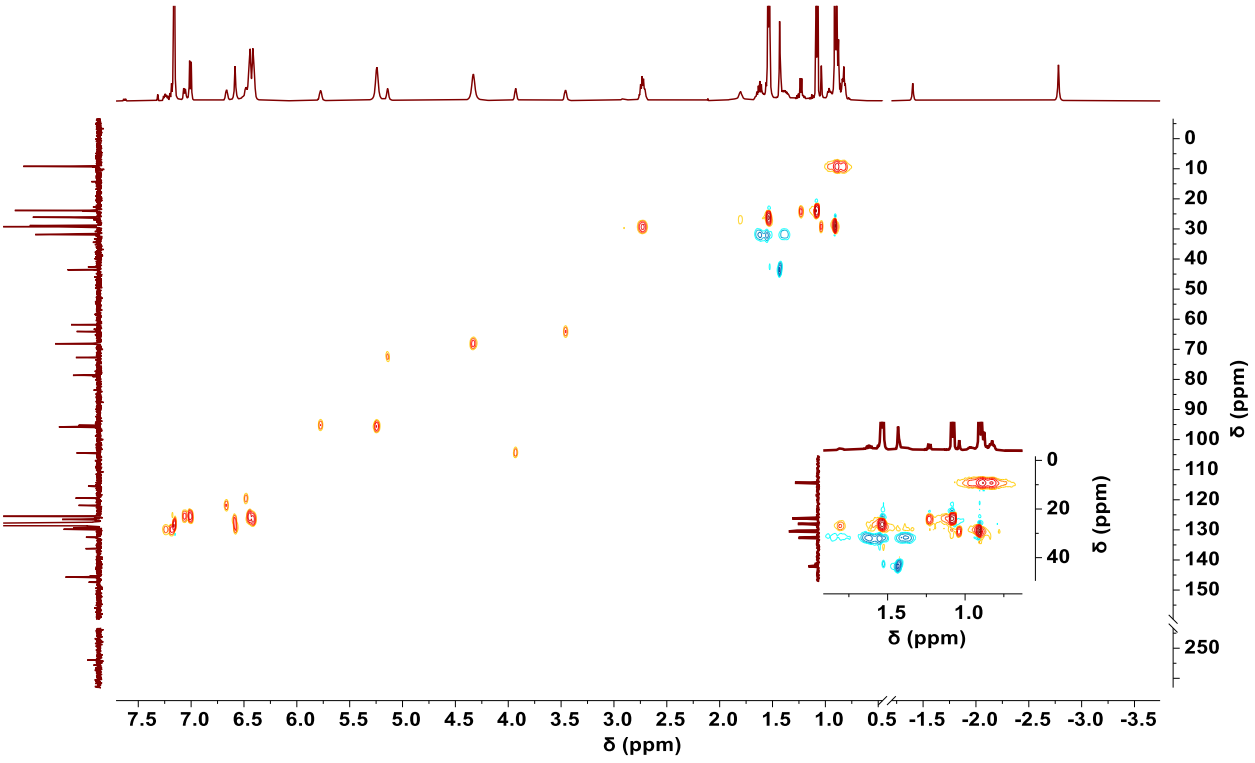


**Figure S4** – Partial $^{1}H/^{13}C$ HSQC NMR Spectrum of **1** (500/126 MHz, $C_6D_6$, 25 °C). The inset shows an enlargement of the aliphatic region of the spectrum.

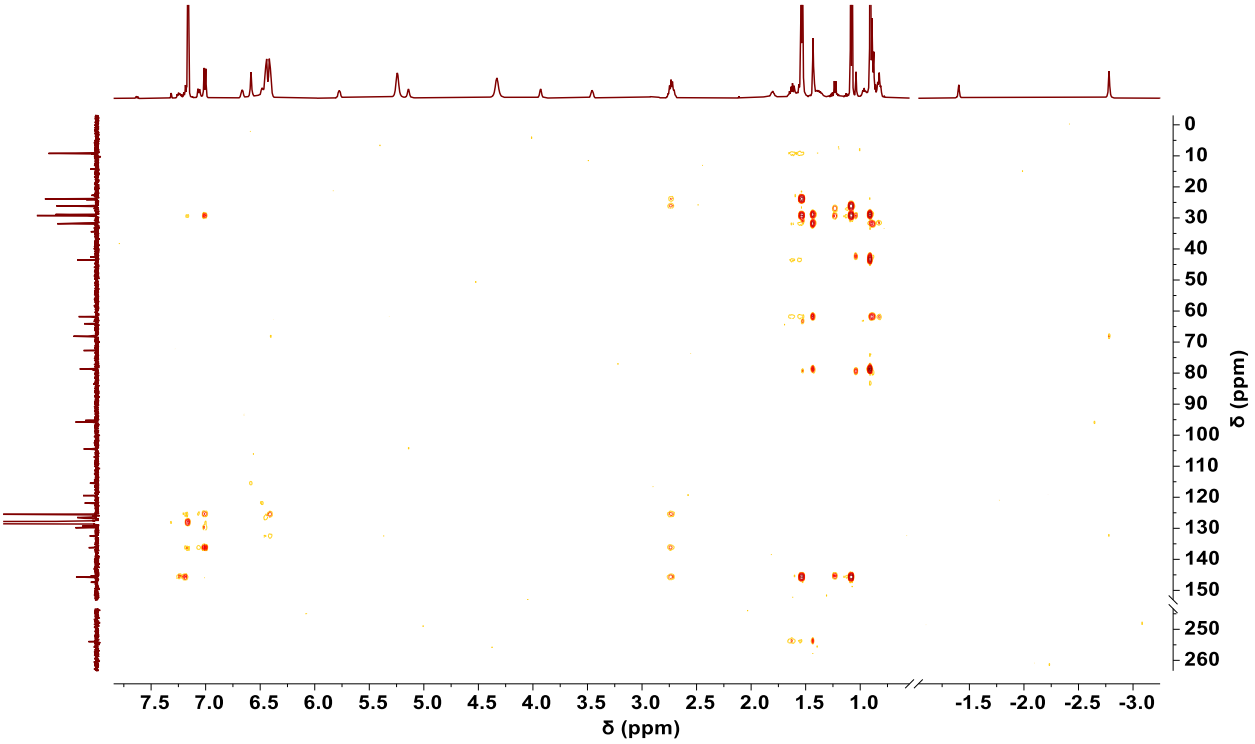


**Figure S5** – Partial $^{1}H/^{13}C$ HMBC NMR Spectrum of **1** (500/126 MHz, $C_6D_6$, 25 °C).

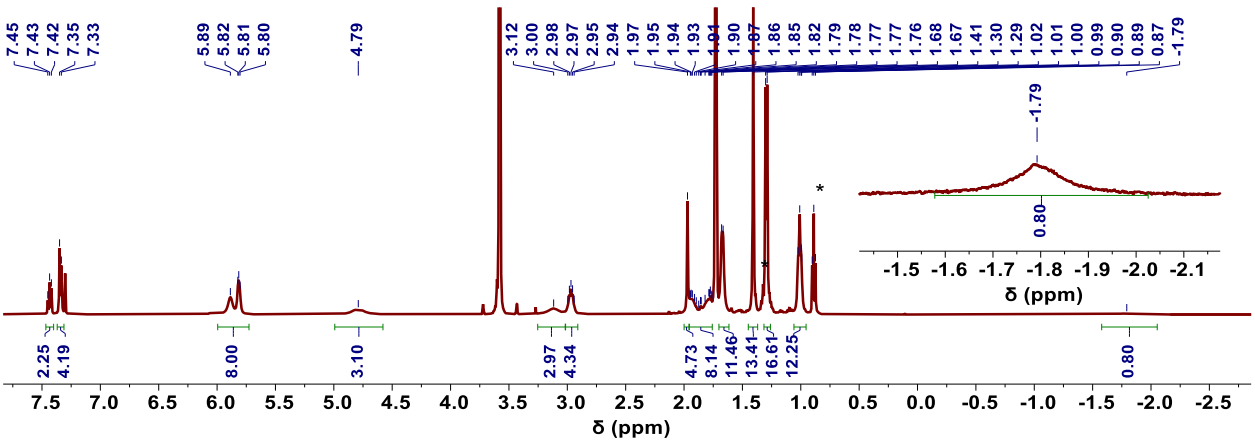


**Figure S6 –** $^{1}H$ NMR Spectrum of **2** (500 MHz, THF-$d_8$, 25 °C). The inset shows enlargement of the hydride region of the spectrum. Note that the asterisks correspond to a pentane impurity.

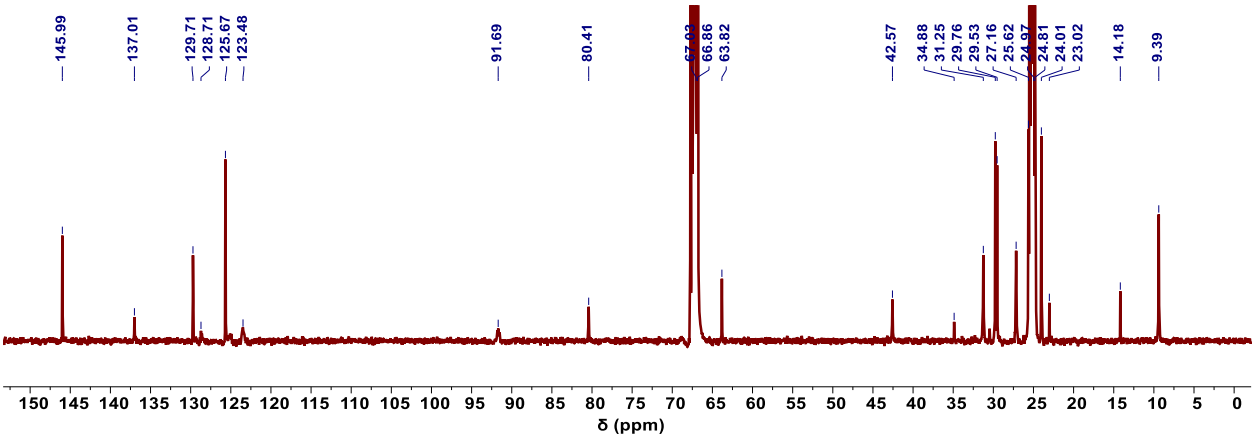


**Figure S7 –** $^{13}C\{^{1}H\}$ NMR Spectrum of **2** (126 MHz, THF-$d_8$, 25 °C). Note: No resonances were observed downfield of 150 ppm.

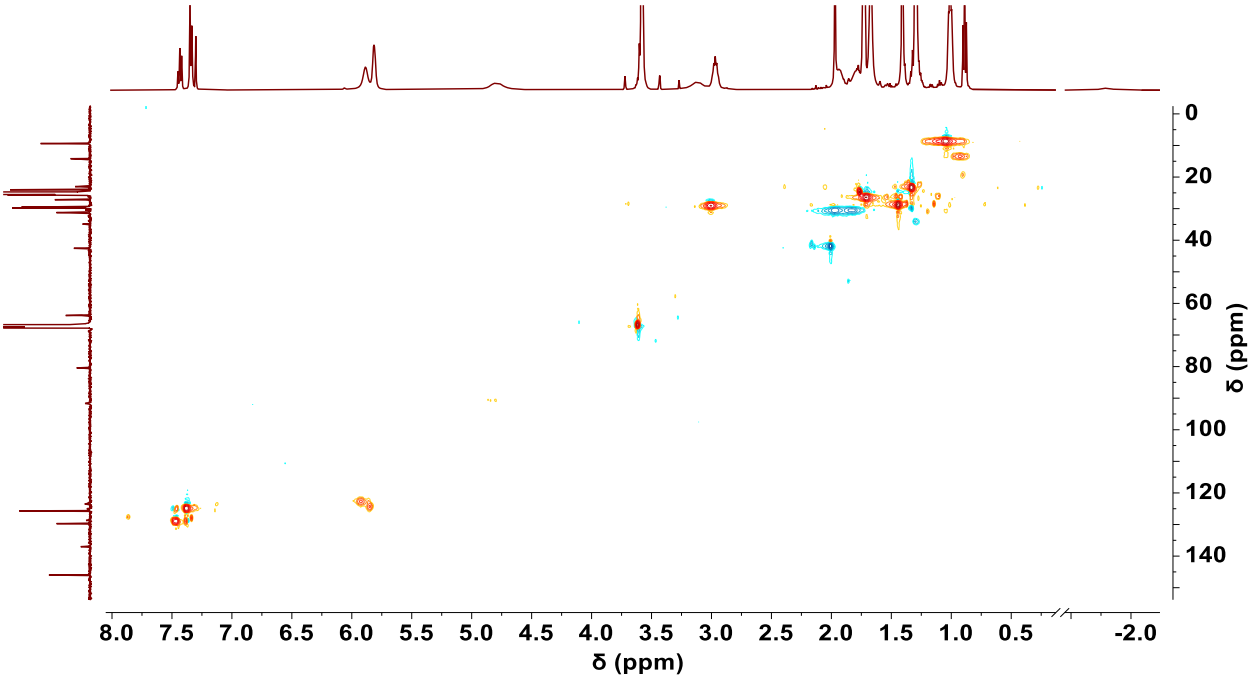


**Figure S8 –** Partial $^{1}H/^{13}C$ HSQC NMR Spectrum of **2** (500/126 MHz, THF-$d_8$, 25 °C).

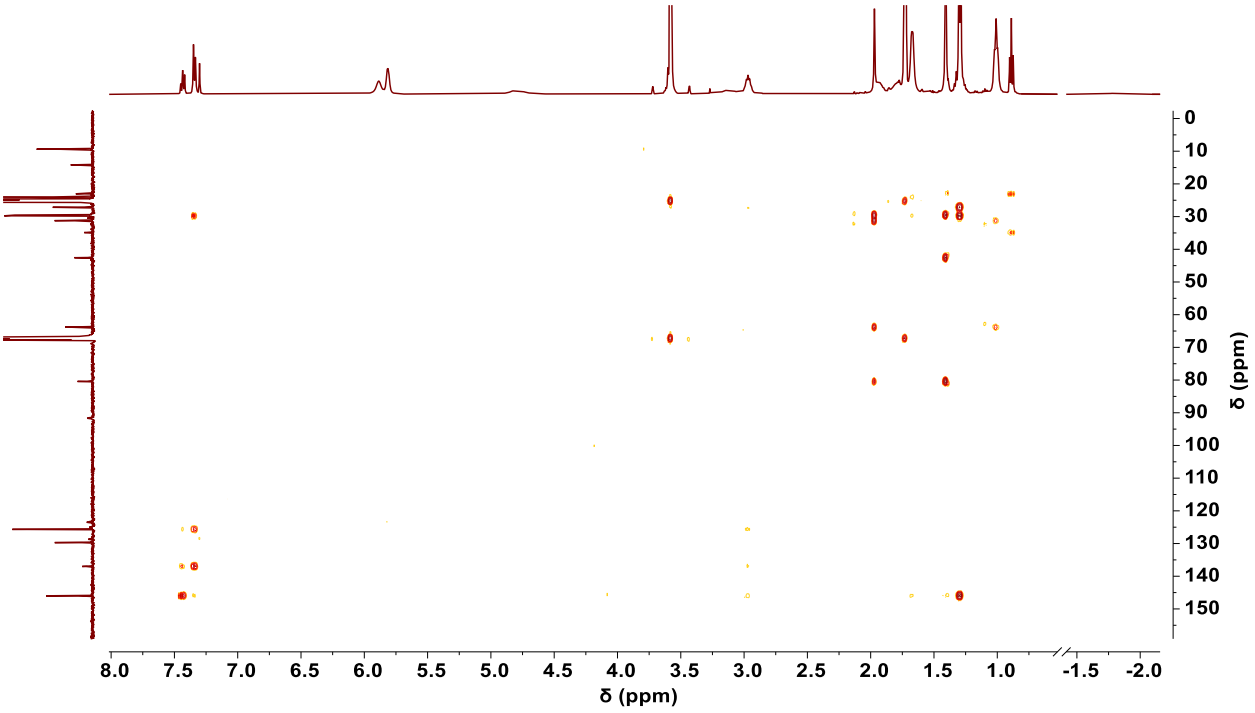


**Figure S9** – Partial $^{1}H/^{13}C$ HMBC NMR Spectrum of **2** (500/126 MHz, THF-$d_8$, 25 °C).

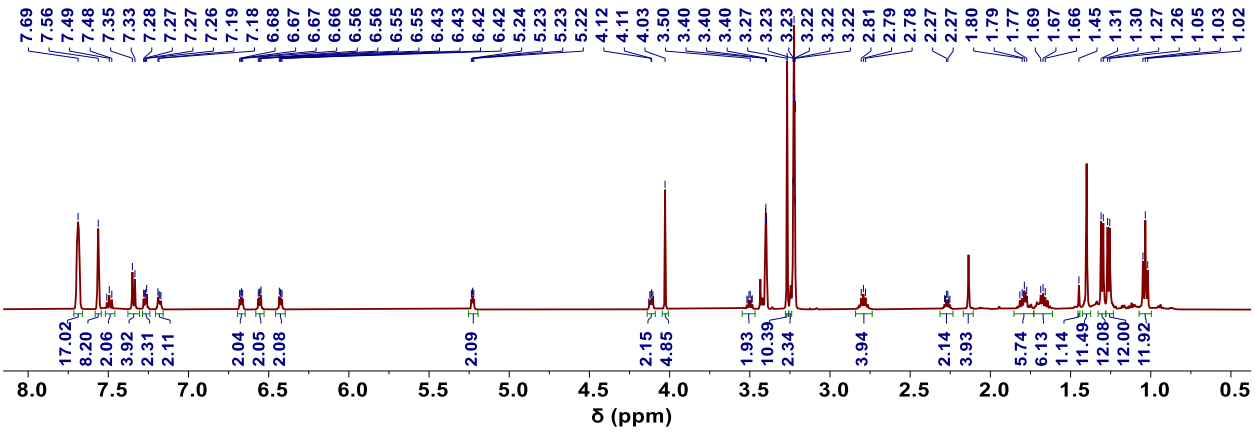


**Figure S10** – $^{1}H$ NMR Spectrum of **3** (500 MHz, DME-$d_{10}$, 25 °C).

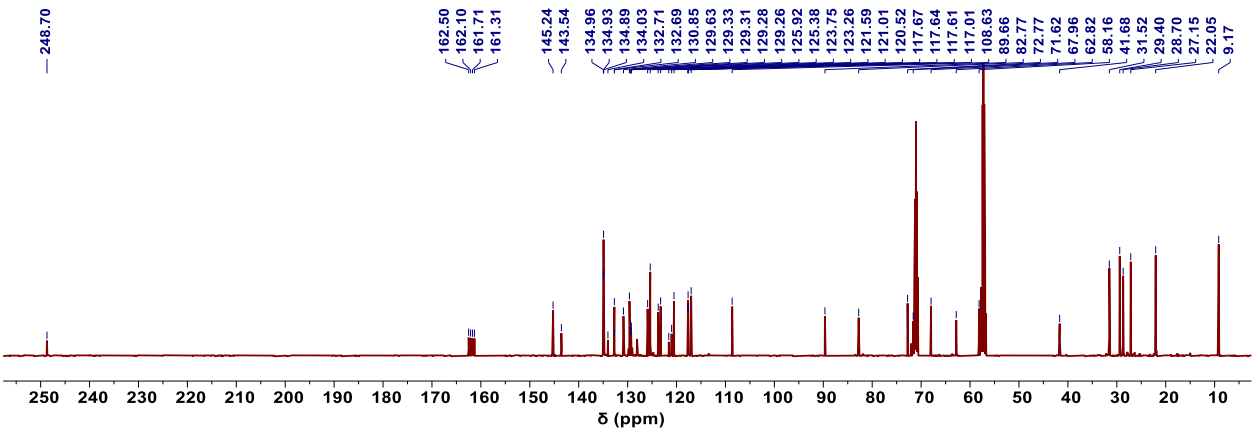


**Figure S11** – $^{13}C\{^{1}H\}$ NMR Spectrum of **3** (126 MHz, DME-$d_{10}$, 25 °C).

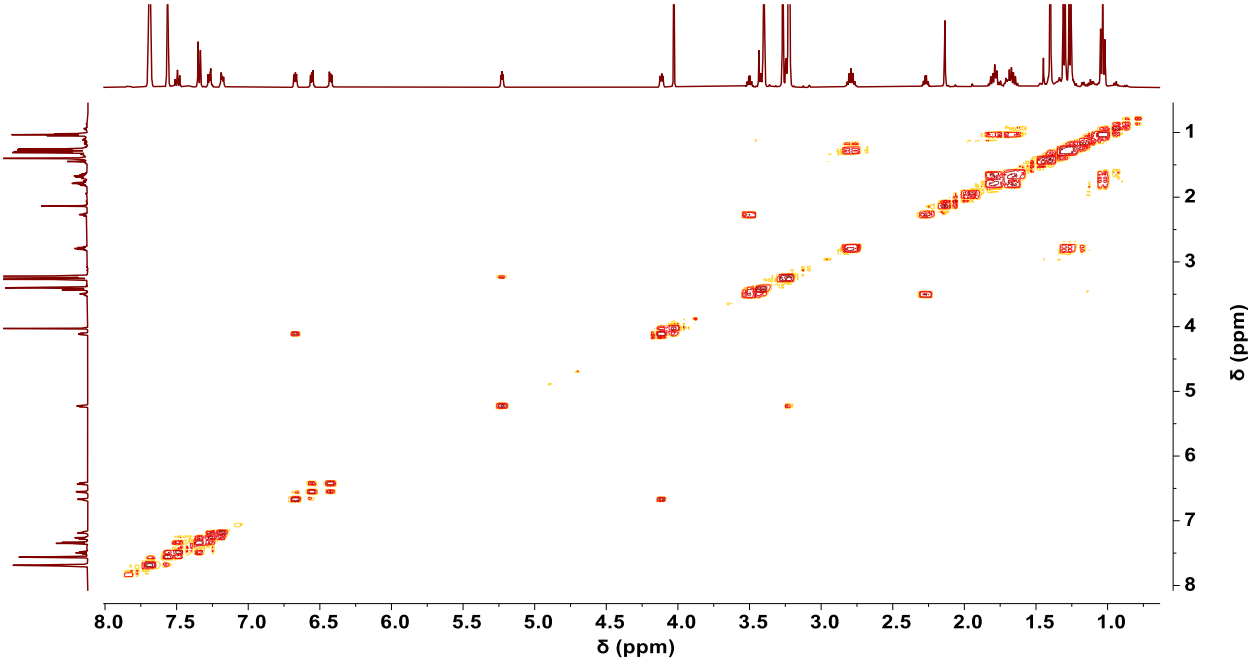


**Figure S12** – $^{1}H/^{1}H$ COSY NMR Spectrum of **3** (500 MHz, DME-$d_{10}$, 25 °C).

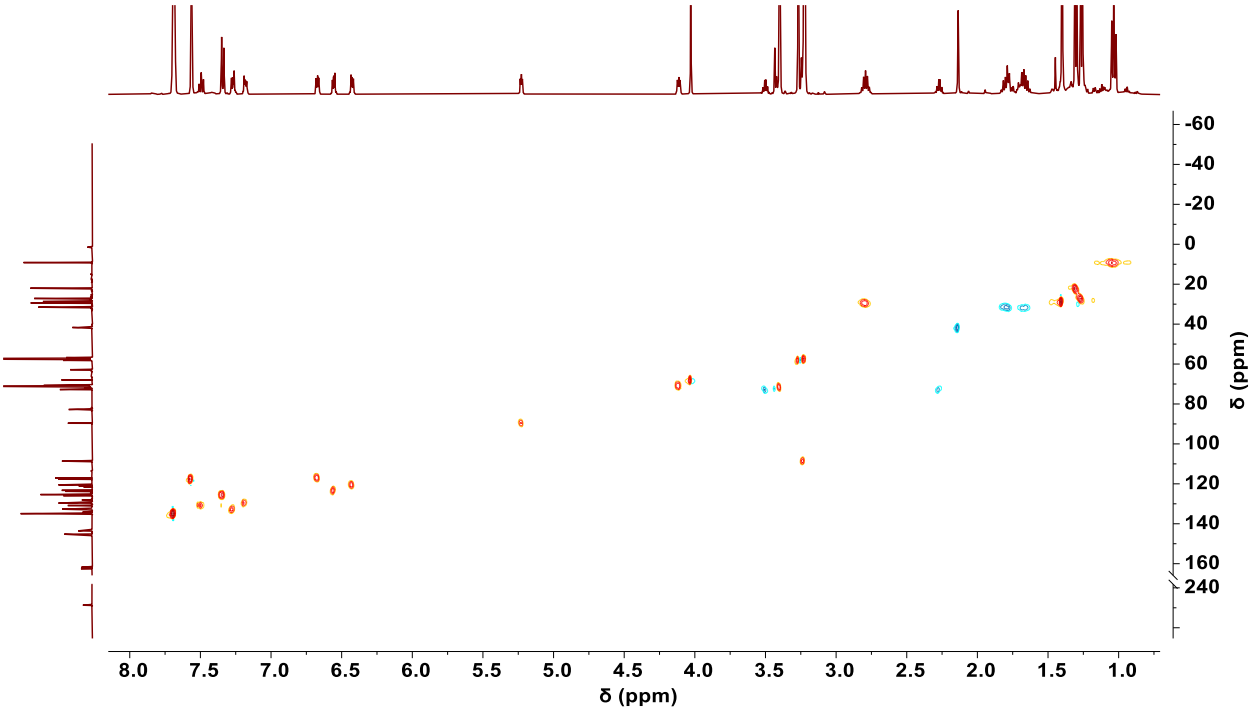


**Figure S13** – Partial $^{1}H/^{13}C$ HSQC NMR Spectrum of **3** (500/126 MHz, DME-$d_{10}$, 25 °C).

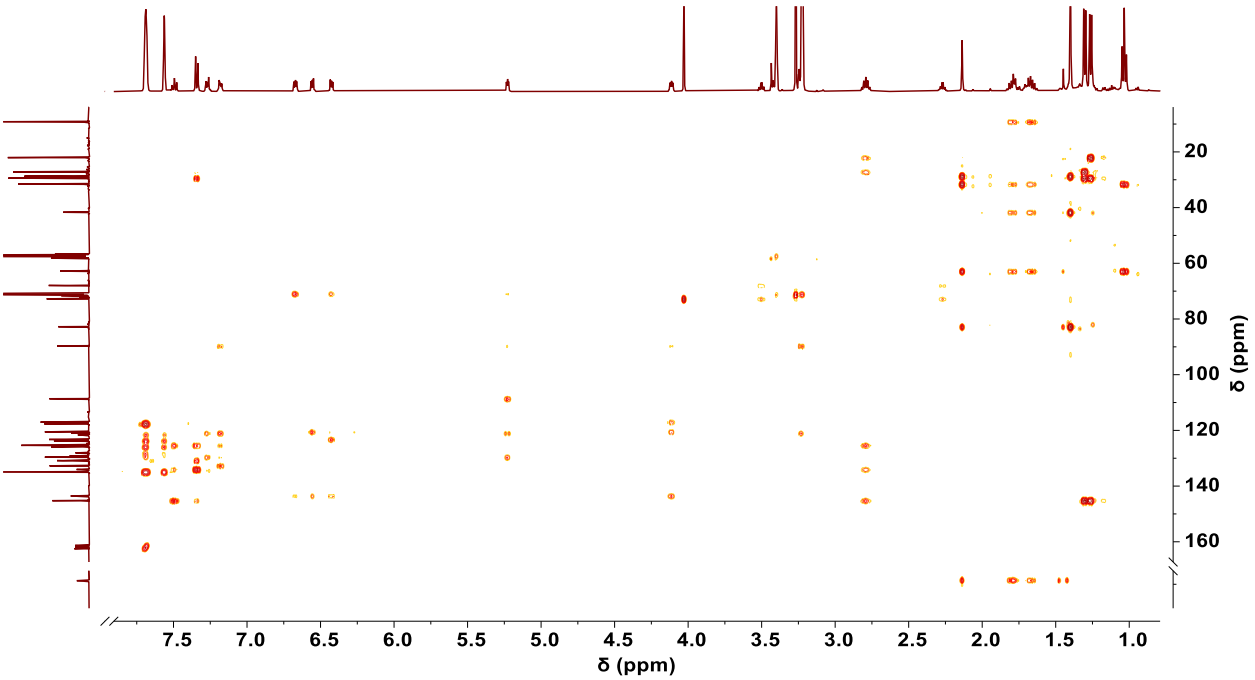


**Figure S14** – Partial $^{1}H/^{13}C$ HMBC NMR Spectrum of **3** (500/126 MHz, DME-$d_{10}$, 25 °C).

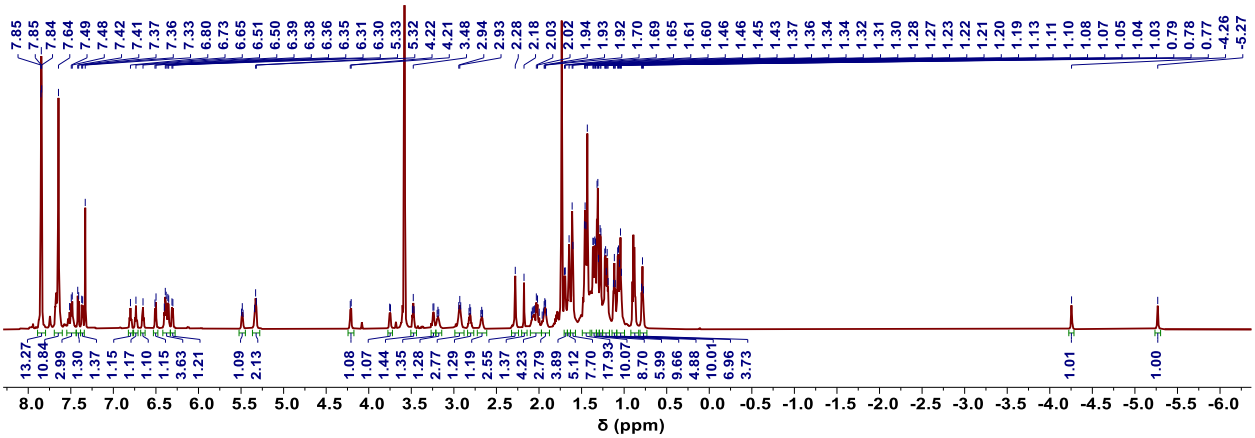


**Figure S15** – $^{1}$H NMR Spectrum of **4** (700 MHz, THF-$d_8$, −35 °C).

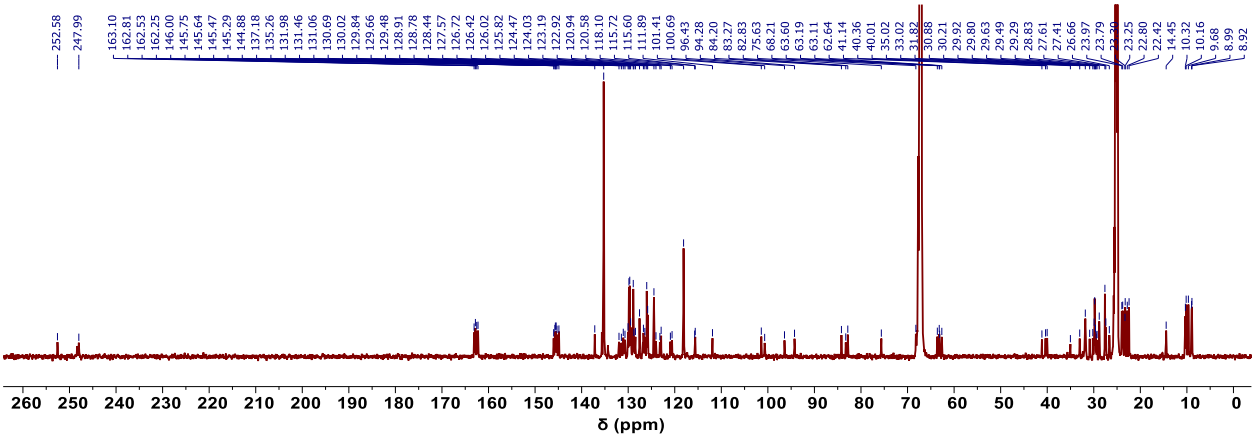


**Figure S16** – $^{13}$C{$^{1}$H} NMR Spectrum of **4** (176 MHz, THF-$d_8$, −35 °C).

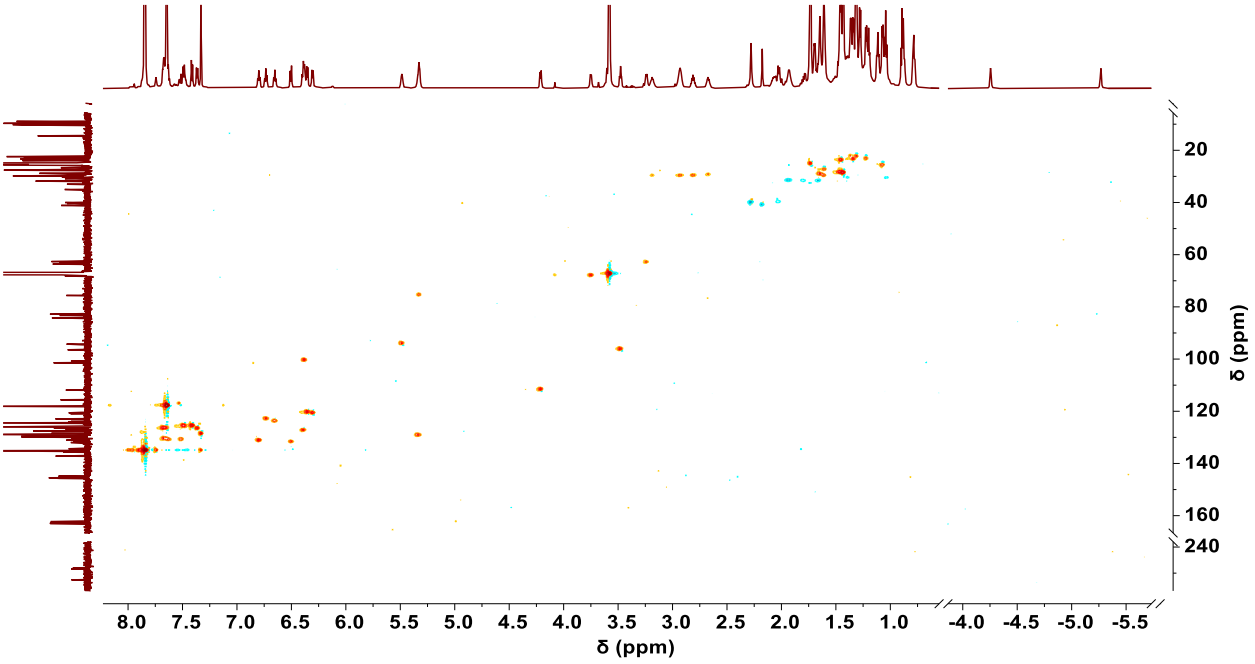


**Figure S17** – Partial $^{1}H/^{13}C$ HSQC NMR Spectrum of **4** (700/176 MHz, THF-$d_8$, −35 °C).

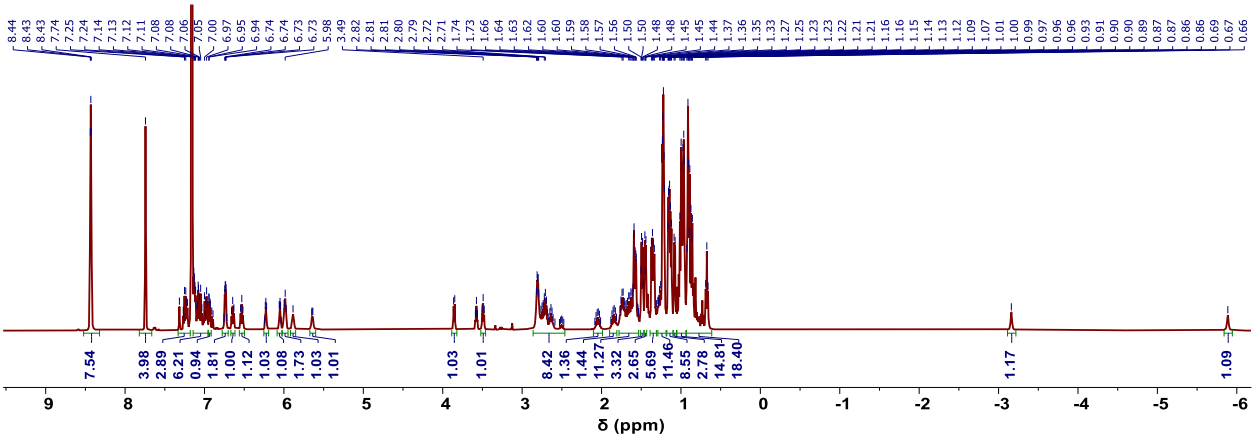


**Figure S18** – $^{1}H$ NMR Spectrum of **5** (500 MHz, $C_6D_6$, 25 °C).

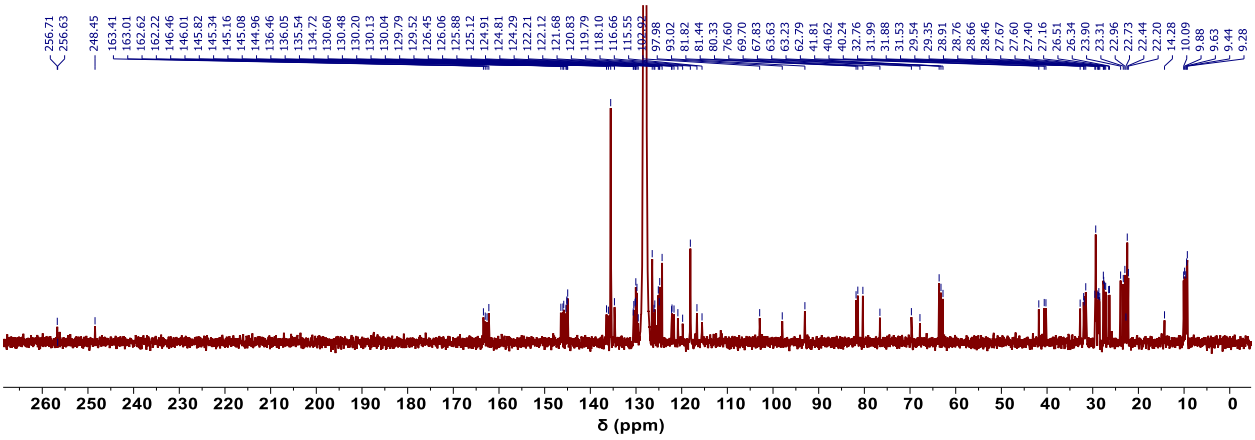


**Figure S19** – $^{13}C\{^{1}H\}$ NMR Spectrum of **5** (126 MHz, $C_6D_6$, 25 °C).

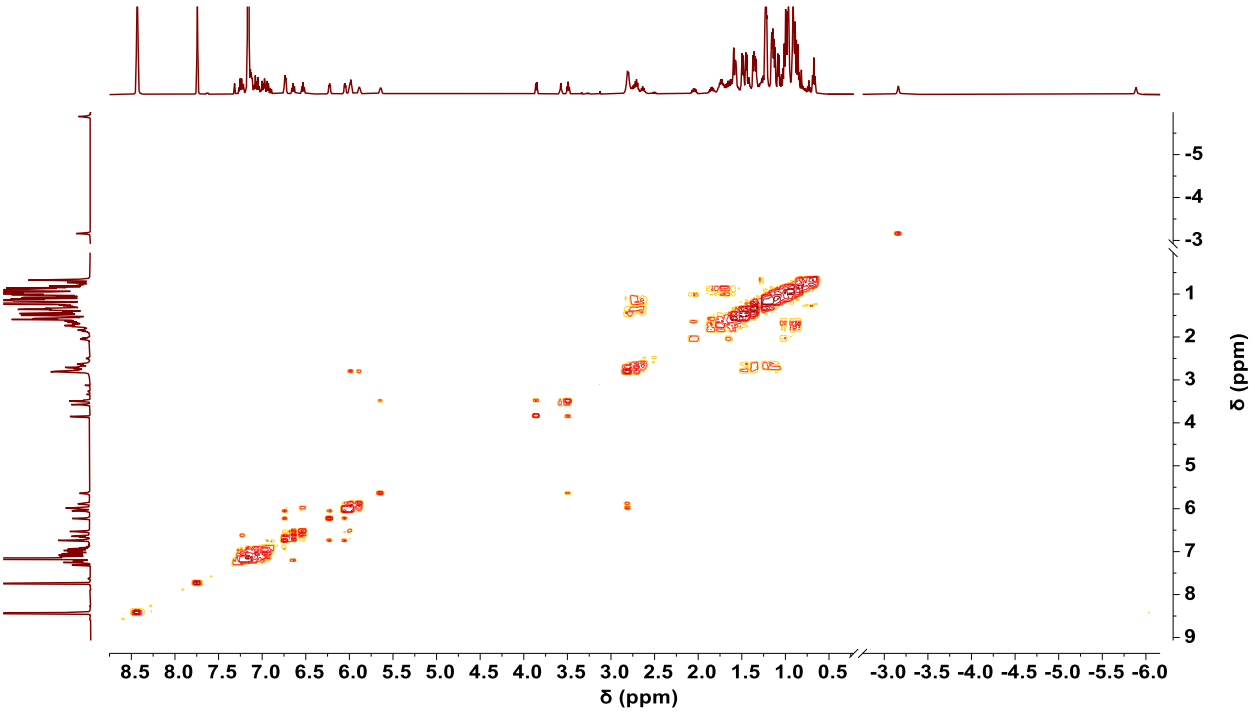


**Figure S20** – Partial $^{1}H/^{1}H$ COSY NMR Spectrum of **5** (500 MHz, $C_6D_6$, 25 °C).

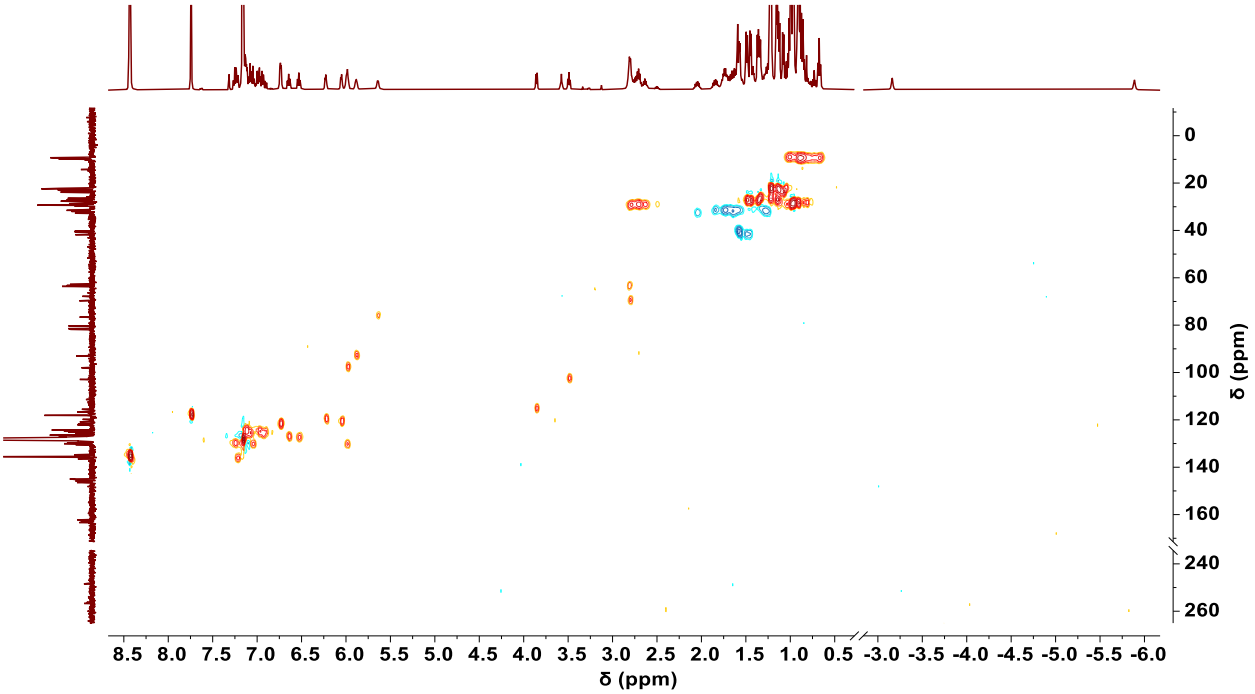


**Figure S21** – Partial $^{1}H/^{13}C$ HSQC NMR Spectrum of **5** (500/126 MHz, $C_6D_6$, 25 °C).

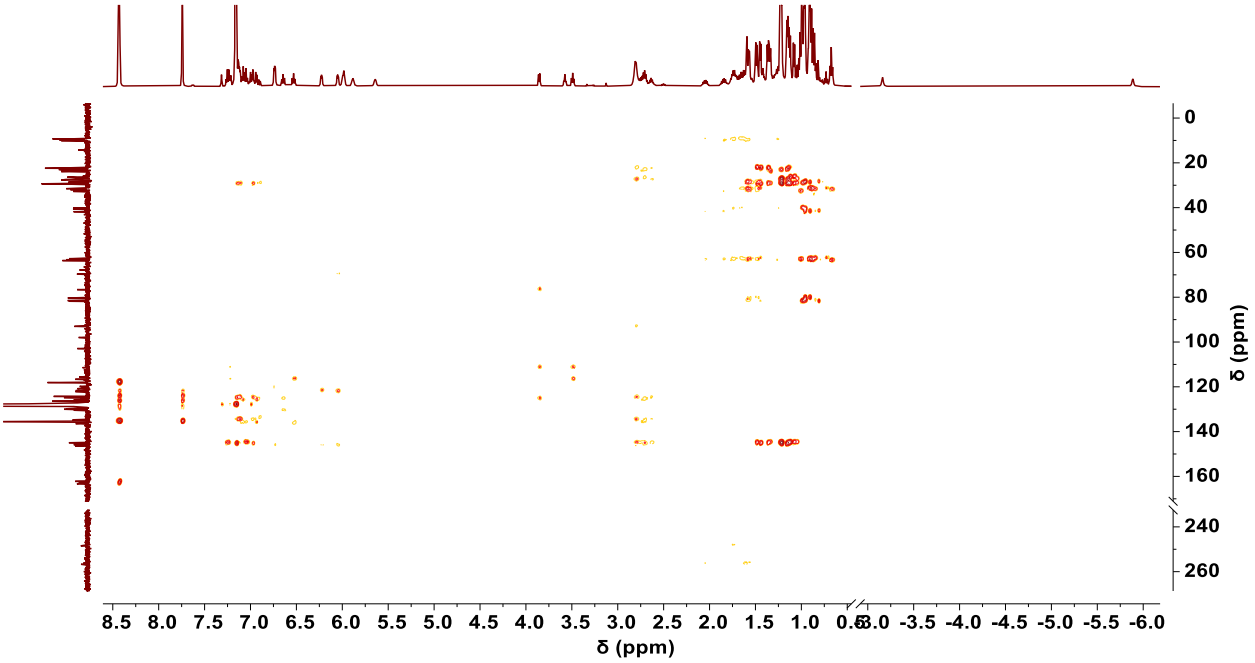


**Figure S22** – Partial $^{1}H/^{13}C$ HMBC NMR Spectrum of **5** (500/126 MHz, $C_6D_6$, 25 °C).

## *Additional Experiments and NMR Spectra*

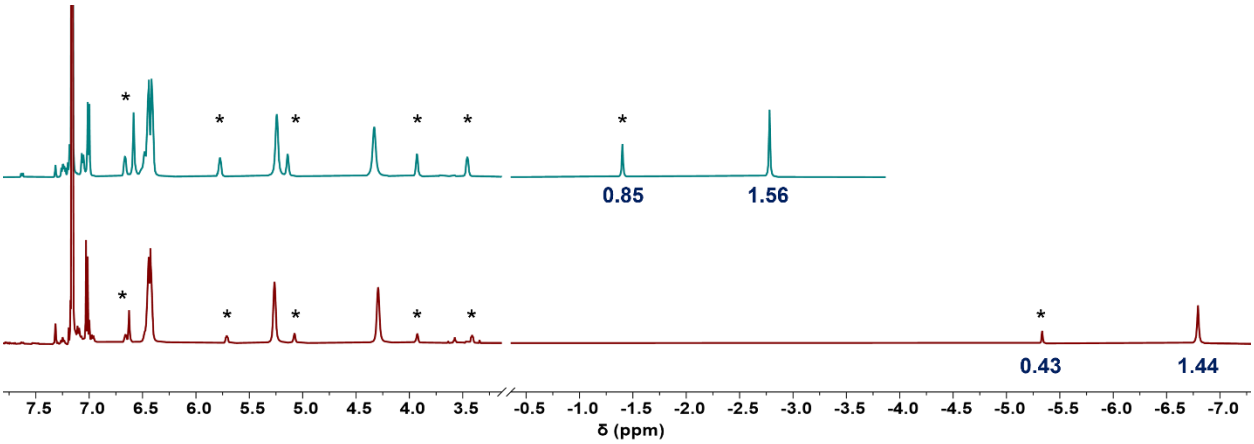


**Figure S23** – Partial $^{1}$H NMR Spectrum of **1** (top) and **1**$^{Cu}$ (bottom) (500 MHz, $C_6D_6$, 25 °C). Signals corresponding to the minor (anti) conformations are designated with asterisks.

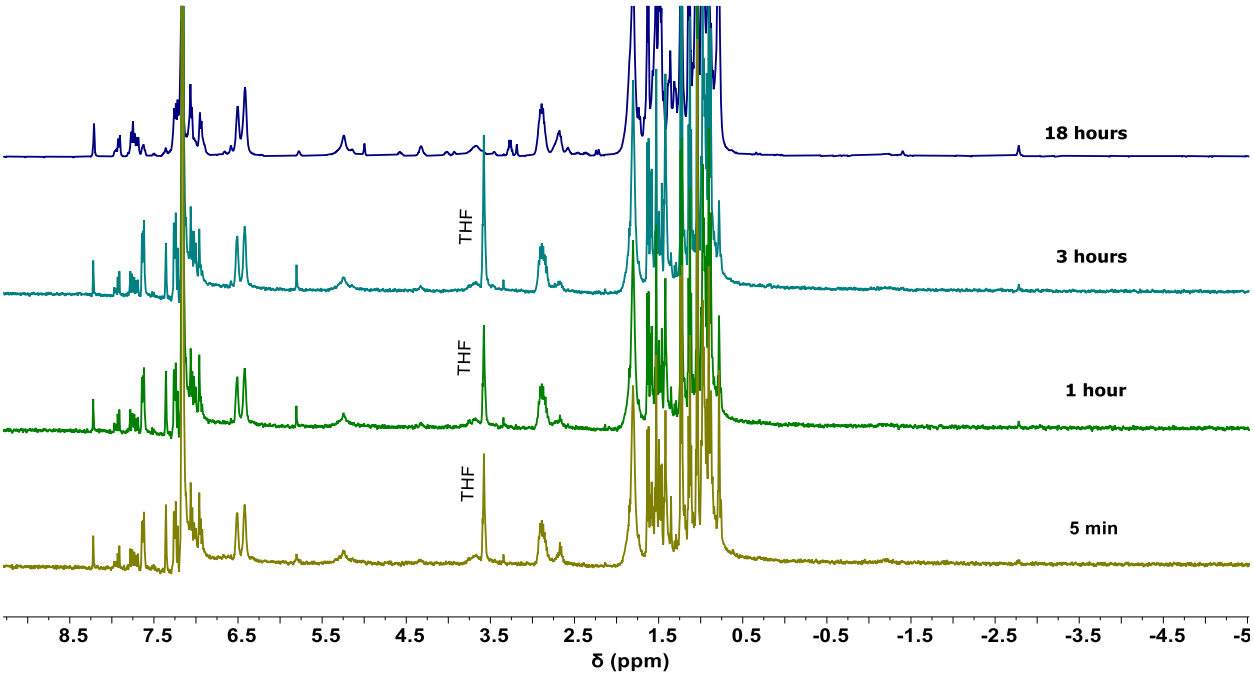


**Figure S24** – Stacked $^{1}$H NMR spectra (400 MHz, $C_6D_6$, 25 °C) of timepoints (see labels on each spectrum) of the reaction between CAACAuCl and $Ta(naph)_3^-$. For each timepoint, an aliquot was removed from the reaction mixture, filtered, and dried *en vacuo* before being re-dissolved in $C_6D_6$ for analysis by $^{1}$H NMR spectroscopy. These spectra show no intermediates and a steady increase in product formation (complexes **1** and **2**) over time.

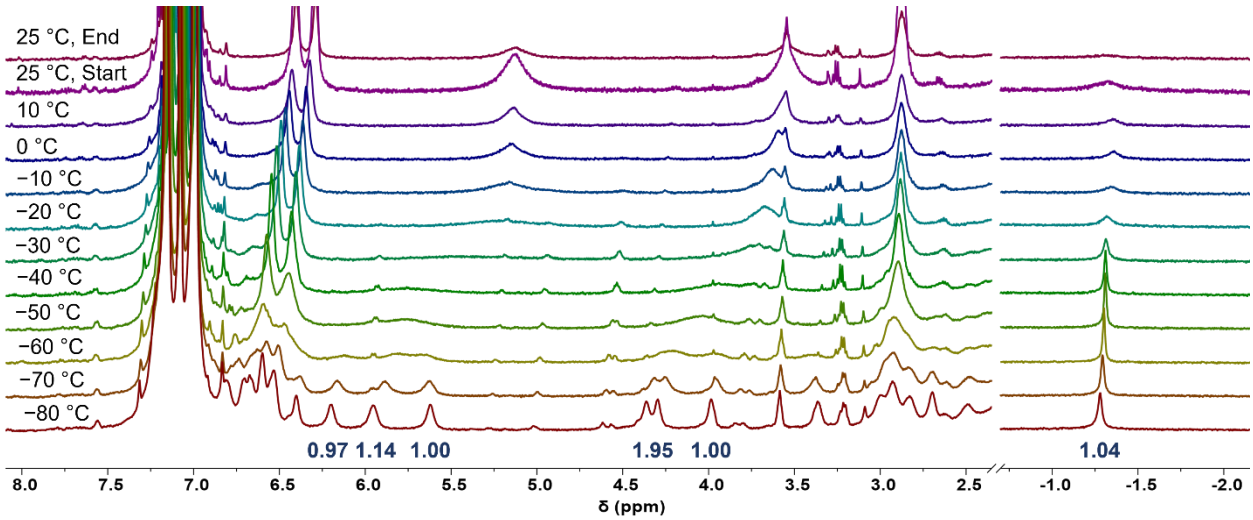


**Figure S25** – Variable temperature partial $^{1}$H NMR spectra of **2** (500 MHz, toluene-$d_8$) ranging from 25 °C (top) to −80 °C (bottom). The topmost spectrum was collected at 25 °C after the variable temperature data, corroborating that there were no irreversible chemical changes during the experiment. Note that integrations are provided for resolved hydride and naphthyl signals in the low temperature (–80 °C) spectrum.

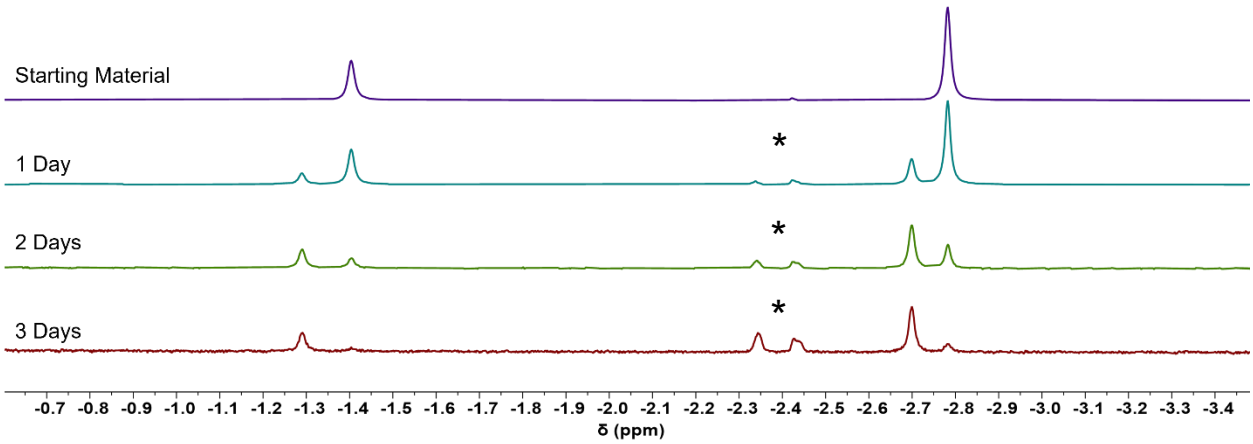


**Figure S26** – Partial H/D exchange of **1** under 1 atm. of $D_2$ at room temperature over 3 days. The hydride regions of the $^{1}$H NMR spectra (400 MHz, $C_6D_6$, 25 °C) show new signals corresponding to a mixed H/D bimetallic (**1**$^{H/D}$) upon deuteride incorporation. Asterisks designate an unknown reaction byproduct.

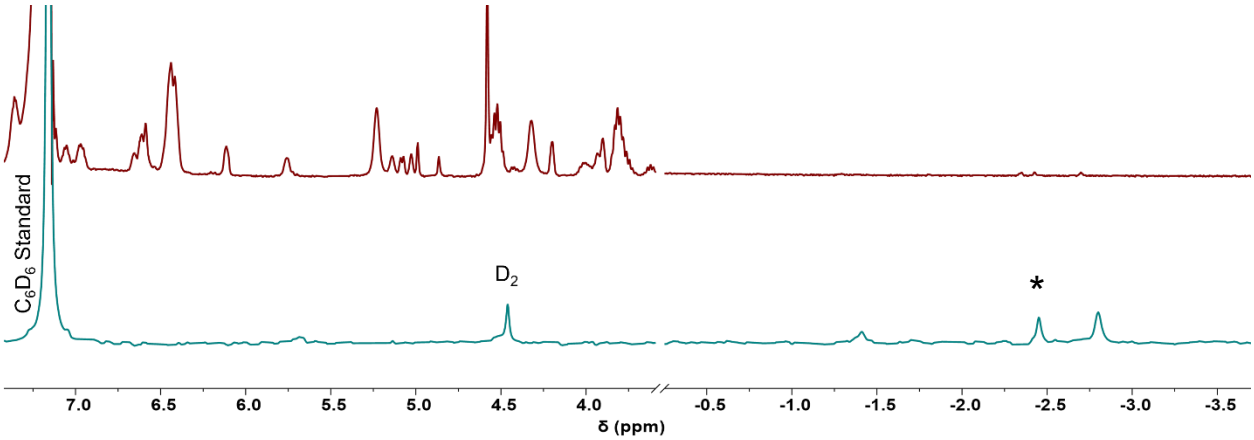


**Figure S27** – Partial $^{1}H$ NMR Spectrum (top) and $^{2}H$ NMR spectrum (bottom; 700 MHz ($^{1}H$)/107 MHz ($^{2}H$), $C_6H_6$ with an internal $C_6D_6$ standard, 25 °C) of **1** + $D_2$ at 45 °C for 1 day, showing full hydride for deuteride exchange. The asterisk designates an unknown reaction byproduct.

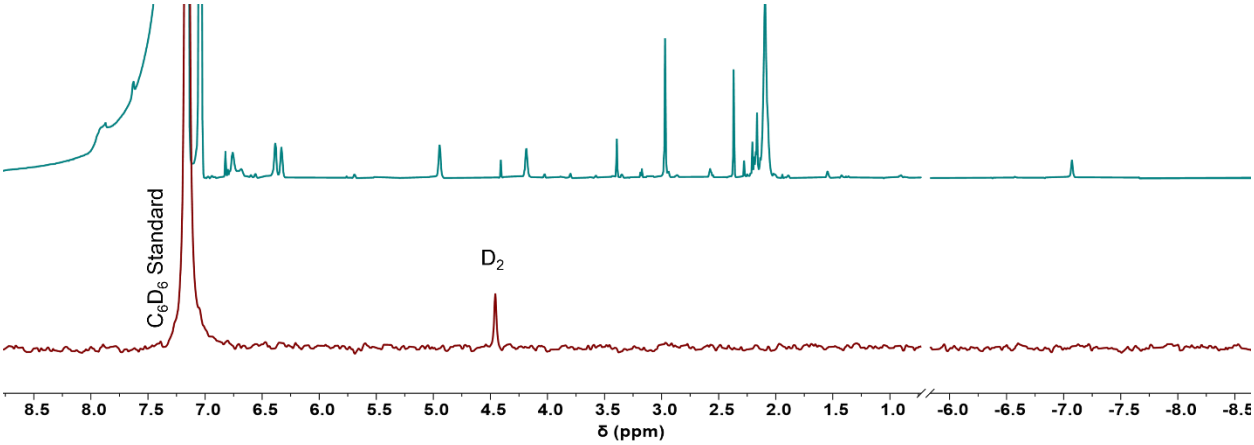


**Figure S28** – Partial $^{1}H$ NMR Spectrum (top) and $^{2}H$ NMR spectrum (bottom; 700 MHz ($^{1}H$)/107 MHz ($^{2}H$), $C_6H_6$ with an internal $C_6D_6$ standard, 25 °C) of $SIMesCuH_2Ta(naph)_2$ + $D_2$ at 65 °C for 3 days, showing no reaction.

## Additional Discussion Related to H/D Exchange Chemistry:

We were unsuccessful in determining whether the hydride ligands in **1** are best considered hydridic or acidic due to the reactive nature of this complex. Complex **1** was reacted with benzyl potassium and HBArF to probe for hydride ligand acidity and basicity, respectively. The reaction with benzyl potassium resulted in an intractable mixture with no spectroscopic evidence for Ta-bound naphthalene groups. The reaction with HBArF resulted in several products; however, by extracting the crude reaction mixture with benzene, a hydride containing species with bound naphthyl protons was obtained as a very minor product. Based on the apparent symmetry of the naphthalene rings, the hydride likely integrates to two suggesting the reaction is more complex than a simple protonolysis. Since intractable reactions occurred with both an acid and a base, we cannot definitively comment on whether the hydrides in complex **1** are best characterized as acidic or hydridic.

Furthermore, both oxidative addition and σ bond metathesis are reasonable mechanisms for the observed H/D exchange reactivity of complex **1**. Either mechanism would result in the formation of HD, which we were unable to observe by $^{1}H$ or $^{2}H$ NMR spectroscopy at these reaction scales. Without any experimental support we refrain from speculating as to the operative mechanism; however, the observation that **1** performs H/D exchange while $\mathbf{1}^{Cu}$ does not may suggest that H/D exchange occurs via an oxidative addition process enabled by decreased steric pressure in the Ta/Au congener. The relative steric environment of the Au and Cu complexes is supported by the syn:anti ratios of the atropisomers as discussed in the manuscript.

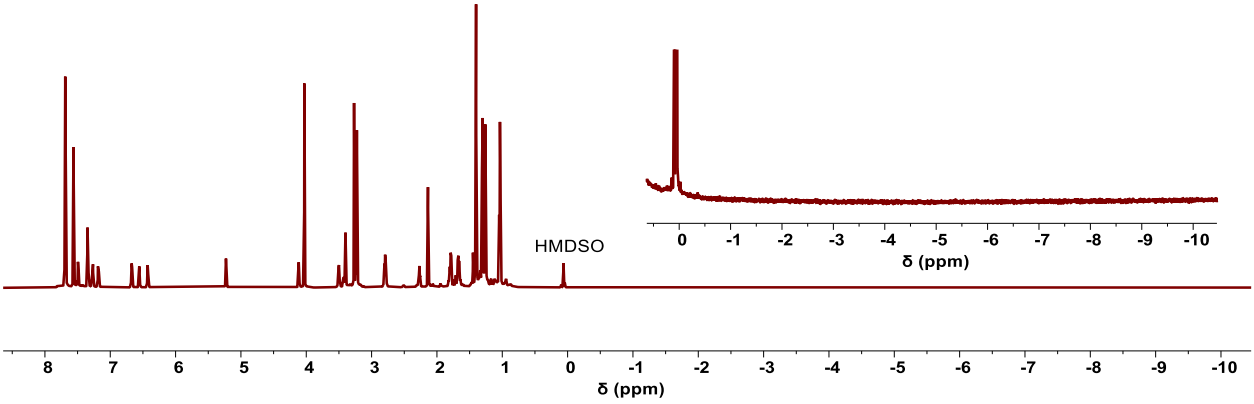


**Figure S29** – Full $^{1}H$ NMR Spectrum of **3** (700 MHz, DME-$d_{10}$, 25 °C) showing no negatively shifted hydride signals. The inset shows an enlargement of the high field spectral region, with the HMDSO peak included for relative scale.

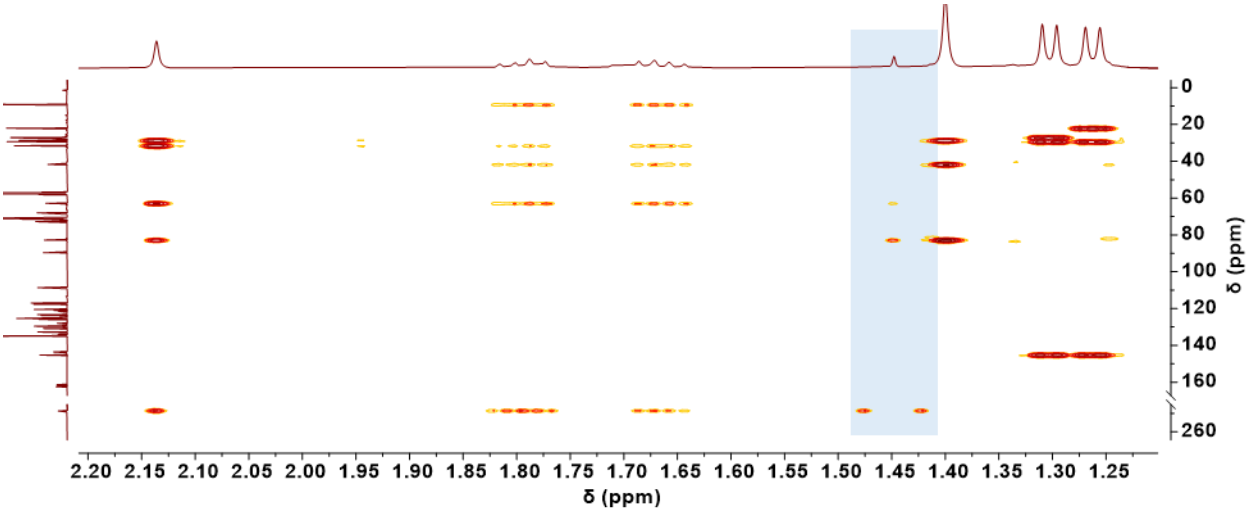


**Figure S30** – Enlarged partial $^{1}H/^{13}C$ HMBC NMR Spectrum of **3** (500/126 MHz, DME-$d_{10}$, 25 °C) showing coupling of the proton peak at 1.45 ppm to the carbene carbon, CAAC carbon bound to two methyl groups, and the CAAC carbon bound to two ethyl groups. The large $^{2}J_{(C,H)}$ through gold results in splitting of the hydride/carbene carbon cross-peak. These data are most consistent with the assignment of the resonance at 1.45 ppm as a μ-hydrido.

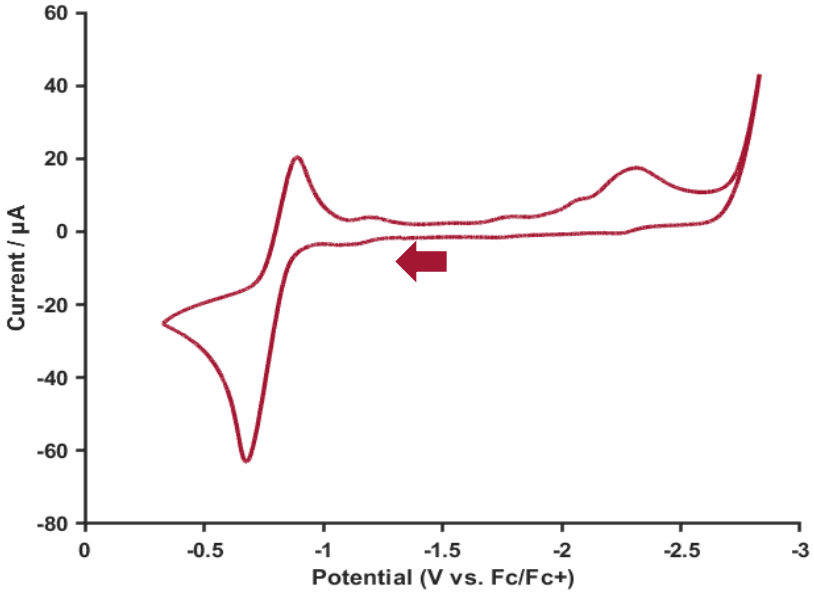


**Figure S31** – Cyclic Voltammogram of **1** in a DME solution (2.40 mM) containing 0.1 M TBABArF at room temperature under $N_2$. The cyclic voltammogram was collected at a scan rate of 200 mV/s. The arrow indicates the direction of the scan, with its tail located at the starting potential (set to the OCP).

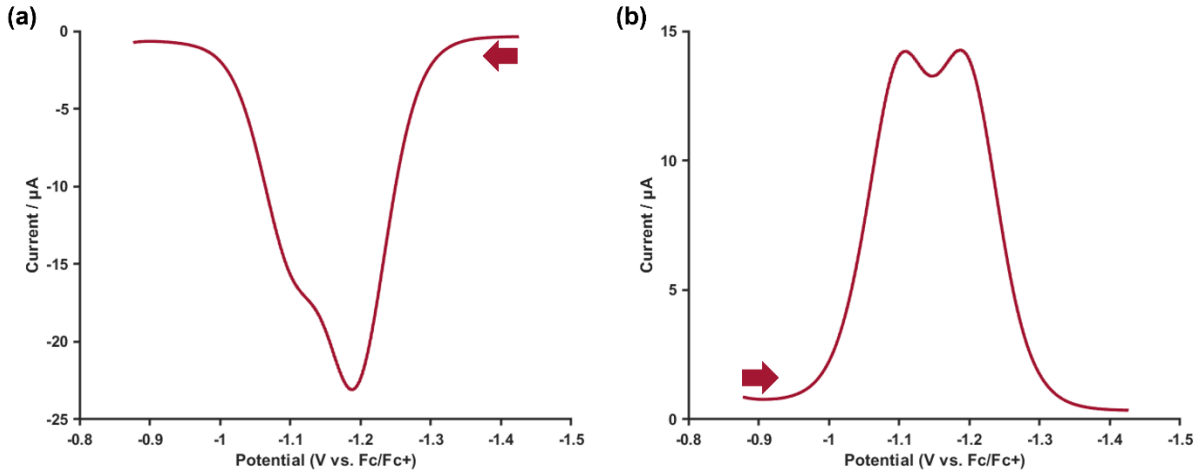


**Figure S32** – Square Wave Voltammograms of **2** in a DME solution (1.65 mM) containing 0.1 M TBABArF at room temperature under $N_2$. The square wave voltammograms were acquired under the following

conditions: increments = 0.001 V, amplitude = 0.025 V, frequency = 15 Hz. The arrows indicate the direction of polarization.

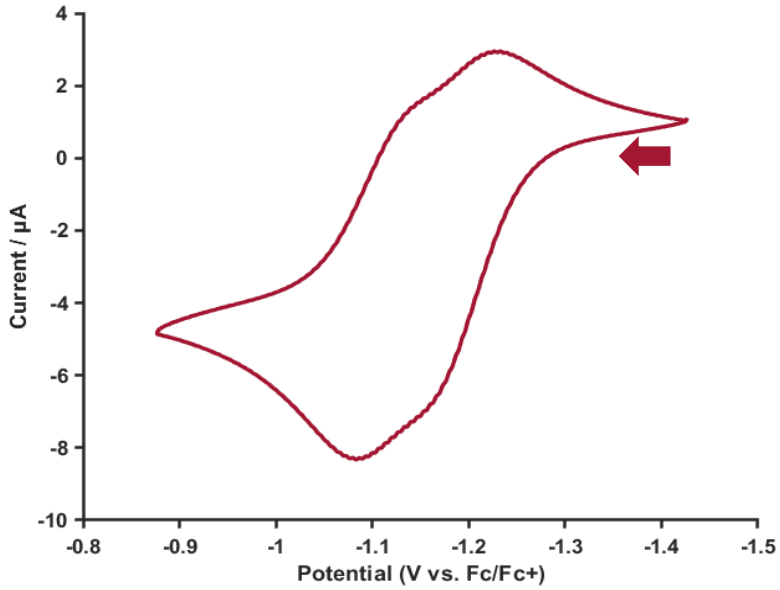


**Figure S33** – Cyclic Voltammogram of **2** in a DME solution (1.65 mM) containing 0.1 M TBABArF at room temperature under $N_2$. The cyclic voltammogram was collected at a scan rate of 50 mV/s. The arrow indicates the direction of the scan, with its tail located at the starting potential (set to the OCP).

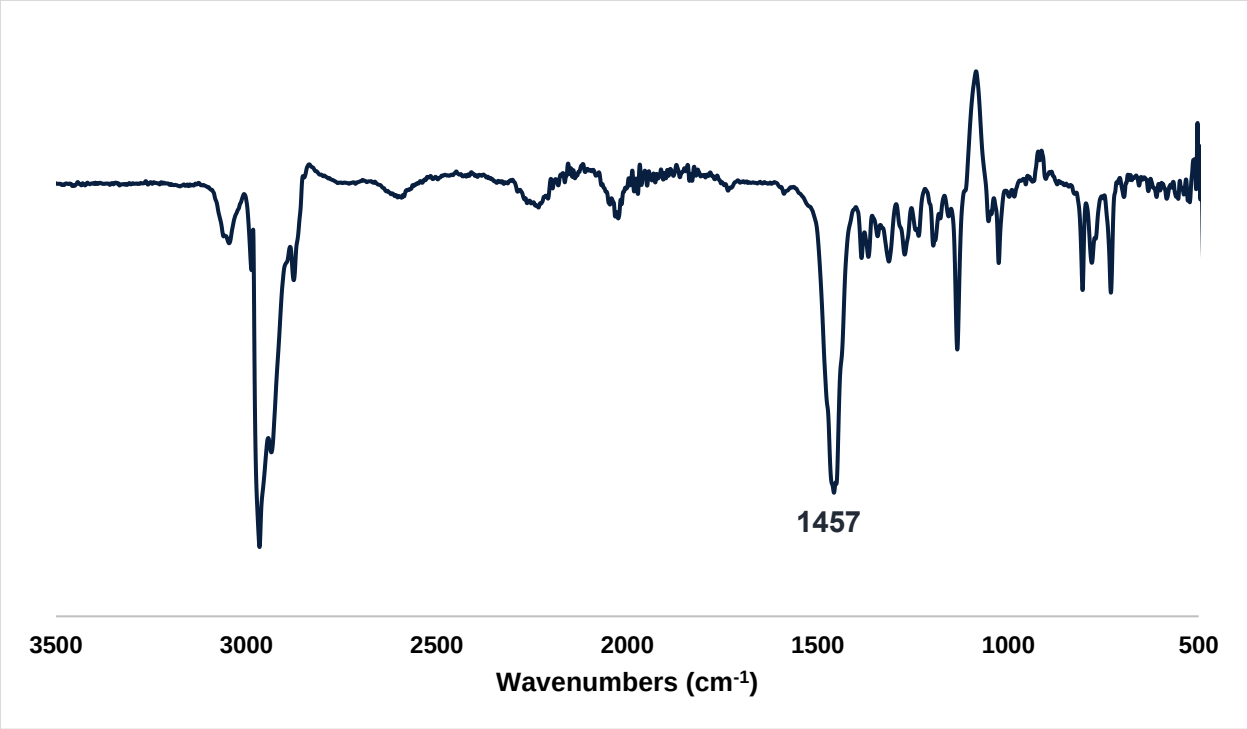


**Figure S34** – FTIR spectrum (diamond ATR) of complex **2**. The stretch at 1457 $cm^{-1}$ is tentatively attributed to the Ta–H–Au stretch based on the DFT predicted Ta–H–Au vibrational mode (1546 $cm^{-1}$). However, the inability to cleanly synthesize deuterated **2** inhibits confirming the hydride stretch via isotopic labeling.

**Table S1** – Substrates utilized for attempted naphthalene exchange from complexes **1**, **2**, **3**, and **4**.

| **1** | **2** | **3** | **4** |
|---|---|---|---|
| Azobenzene | Aniline | 1,2-Bis(diphenylphosphino)ethane | 1,2-Bis(diphenylphosphino)ethane |
| Trimethylphosphine | Anthracene | 2,6-dimethylphenyl isocyanide | 2,6-dimethylphenyl isocyanide |
| 1,2-Bis(diphenylphosphino)ethane | Phenol | Ethylene | Ethylene |
| Ferrocenium Chloride | Diisopropylamine | Cyclooctadiene | Cyclooctadiene |
| Pentafluorophenol | di-p-tolylcarbodiimide | trimethylphosphine | trimethylphosphine |
| 1-azidoadamantane | 2,6-dimethylphenyl isocyanide | | Lithium dimethylamide |
| 2,6-dimethylphenyl isocyanide | Perfluorophenyl azide | | |
| 3,4,5-trifluorophenol | 1-azidoadamantane | | |
| | 3,4,5-trifluorophenol | | |
| | 2,3,5,6-tetrafluorophenol | | |
| | Azobenzene | | |
| | Ferrocenium chloride | | |
| | Diphenyl sulfide | | |

## *Additional Discussion Pertaining to the Structural Assignments of Complexes 2 and 3*

**Complex 2:**

Since we were unable to locate the hydride in the SCXRD structure of complex **2**, we explored alternative structural assignments. From the SCXRD data, we know that **2** is a neutral complex. Moreover, from multinuclear NMR spectroscopy, we know that it is diamagnetic. These observations limit the possible number of hydrides that can be present in the cluster to either one or three. Zero or two hydrides would necessarily result in an open-shell species with a half integer spin (no logical electronic structure consistent with a diamagnet). The integration of the hydride signal (0.80) in the $^{1}$H NMR spectrum of **2** (Figure S6) demonstrates that the data best matches a single hydride ligand. Both SCXRD and DFT data suggest the hydride most likely bridges between the Ta and Au atoms positioned away from the canted naphthalene rings. The canting of the naphthalene rings away from the bridging hydride is well-reproduced in the DFT calculations, as seen in the HOMO of complex **2** in Figure 5.

To further support the hydride location bridging between Ta and Au, we performed DFT calculations to optimize the hydride between the two gold atoms on **2** (*ie.* **2'**; Figure S37). Related carbene-supported [Au-μH-Au]$^{+}$ units are known (see Figure S44 and the associated discussion) and we wanted to rule out this structural possibility. The optimization resulted in significant elongation of one Ta–Au bond (3.322 Å) and contraction of another (2.715 Å), deviating significantly from the SCXRD data. Said experimental data are reproduced most faithfully with the hydride placed bridging Ta and Au.

Additionally, in the $^{1}$H NMR spectrum of **2** at −80 °C (Figure S25) the integrations of resolved naphthalene signals and the hydride resonance show a relative integration of one for the hydride. An alternative interpretation of these data may be that, upon cooling, multiple asymmetric hydrides are resolved. However the hydride signal only shifts 0.04 ppm (downfield) as it cools from 25 °C to −80 °C, which is inconsistent with additional hydride signals being present in the aliphatic region of the low temperature spectrum, as they would coalesce at higher temperatures (intermediate exchange regime on the NMR timescale) and result in a much larger shift of the hydride signal as a function of temperature.

Whereas we were unable to locate the hydride in the SCXRD structure of **2**, our group has synthesized the analogous cluster with SIMes as the ligand on gold instead of EtCAAC, **2$^{\mathbf{SIMes}}$**. In this structure, the hydride ligand can be located in the Fourier difference map in the location posited for **2** (Figure S43). The corresponding $^{1}$H NMR spectrum of **2$^{\mathbf{SIMes}}$** demonstrates an analogous spectral signature to that of the $^{Et}$CAAC congener (**2**); the full synthetic details and complete characterization data for this complex will be published elsewhere.

Overall, the compilation of detailed NMR studies, SCXRD data, and DFT data supports only one structure for **2**, the proposed trimetallic core featuring a single hydride located along one of the Ta–Au bonds.

**Complex 3:**

We were unsuccessful in obtaining suitable single crystals of **3** and have assigned its structure based on NMR spectroscopy data and DFT calculations. The 2D NMR spectra of **3** support our assignment of the peak at 1.45 ppm corresponding to a hydride ligand. The $^{1}H/^{1}H$ COSY shows that this peak does not couple to any other $^{1}H$ peaks in the spectrum, and the $^{1}H/^{13}C$ HSQC shows that this signal does not correspond to a proton bound to a carbon atom. Most importantly the $^{1}H/^{13}C$ HMBC shows coupling of this peak to the carbene carbon ($^{2}J_{(C,H)}$), the CAAC carbon bound to two ethyl groups ($^{3}J_{(C,H)}$), and the CAAC carbon bound to two methyl groups ($^{4}J_{(C,H)}$; Figure S30). These cross-peak positions and relative intensities make sense for a hydride ligand featuring scalar coupling through gold to the Au-bound $^{Et}$CAAC fragment. Additionally, the peaks in the $^{1}H$ NMR spectra clearly integrate to two BArF anions, two $^{Et}$CAAC ligands, and two naphthalene rings. Without a hydride ligand, this would afford a paramagnetic complex, which is inconsistent with the data. Finally, the CV and SWV data suggest a structural change after a one electron oxidation (complex **4**) but there is no evidence of a structural change after the second oxidation event (as clearly indicated by the symmetry of the anodic SWV scan; Figure S32). Holistically, the only reasonable structural assignment of **3** is a trimetallic monohydride, with the hydride signal assigned to the peak at 1.45 ppm.

## *Further Discussion of Formal Oxidation State Assignments*

Proposed Formal Oxidation States of each complex:

**1**: $Au^{1}Ta^{1}$

**2**: $\mathbf{Au^{1}Au^{1}Ta^{-1}}$ or $Au^{1}Au^{0}Ta^{0}$ or $Au^{0}Au^{0}Ta^{1}$

**3**: $Au^{1}Au^{1}Ta^{1}$

**4**: $Au^{1}Au^{1}Ta^{1}$

**5**: $Au^{1}Au^{1}Au^{1}Ta^{1}$

The formal oxidation states of complexes **1**, **3**, **4**, and **5** were assigned as $Au^{1}/Ta^{1}$ for each metal center. These assignments match the charge of each complex (0, +2, +1, +1, respectively) and result in diamagnetic ground states, as observed in the $^{1}H$ NMR spectra.

Complex **2** is more complicated because there are three possible oxidation state assignments that result in a charge-neutral diamagnet: $Au^{1}Au^{1}Ta^{-1}$, $Au^{1}Au^{0}Ta^{0}$, or $Au^{0}Au^{0}Ta^{1}$, with the latter two invoking antiferromagnetic coupling between metal centers. We believe that **2** is best described as $Au^{1}Au^{1}Ta^{-1}$ based on chemical tuition, however we cannot ignore the possibility of alternative oxidation state assignments. The covalency of the strongly coupled multimetallic core convolutes definitive formal oxidation state assignments as is reflected in the DFT data. No additional information could be gleaned from the naphthalene bond metrics from DFT or SCXRD, and Mulliken/Hirschfeld charges did not provide clearer insight (Figure S38).

## *Computational Details*

All calculations were performed using spin-restricted DFT within the Gaussian 16 software suite.[11] Initial geometries were sourced from single-crystal XRD structures. Geometry optimizations were performed using the parameter-free PBE0 functional,[12] including a quasi-relativistic small core pseudopotential for Ta and Au.[13] For **1** and $\mathbf{1^{Cu}}$, a def2-TZVPD basis set was used for Ta and Au/Cu with a def2-SVPD basis set used for all other atoms. For **2**, **2'**, **3**, and **4**, a def2-SVPD basis set was used for all atoms. Similar levels of theory have been successfully applied to related heteromultimetallic systems in the literature.[9b, 14] Grimme's D3 dispersion correction[15] was employed in each case and calculated structures were confirmed as minima by the absence of imaginary vibrational frequencies. Hirshfeld population analysis was utilized to compare relative charges on metal centers in complexes **1**, **2**, and **3**.[16] Multiwfn[17] was utilized (starting from optimized geometries) to calculate bond critical points for the QTAIM analysis. Orbital contours were plotted with a 0.04 $eA^{-3}$ isosurfaces and visualized using GaussView5.[18]

Cartesian coordinates for optimized structures are available as the following .xyz files uploaded as Electronic Supporting Information for this submission:

**1**: Optimized_Coordinates_1.xyz
$\mathbf{1^{Cu}}$: Optimized_Coordinates_1Cu.xyz
**2**: Optimized_Coordinates_2.xyz
**2'**: Optimized_Coordinates_2'.xyz
**3**: Optimized_Coordinates_3.xyz
**4**: Optimized_Coordinates_4.xyz

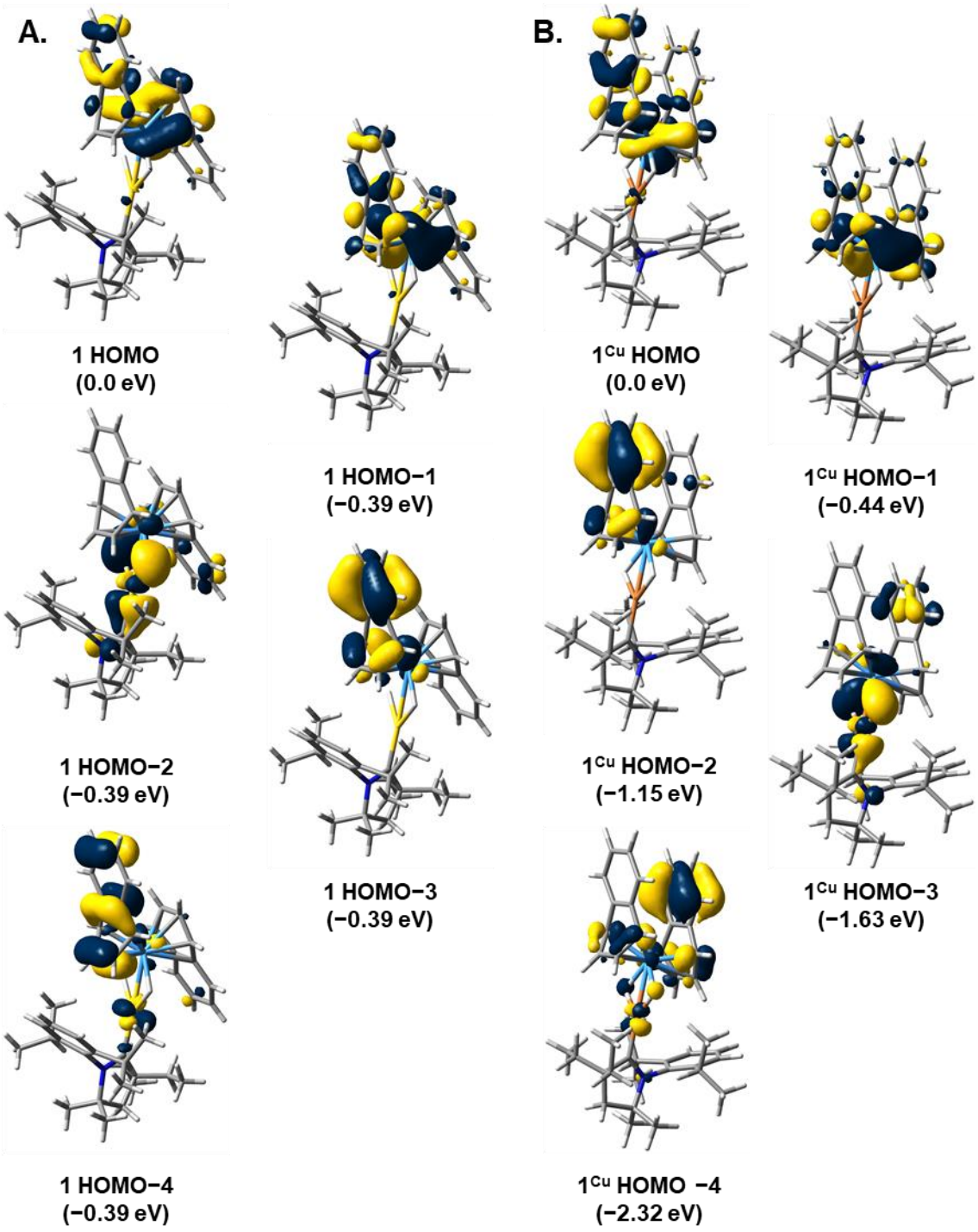


**Figure S35** – Frontier Kohn-Sham orbitals for TaAu bimetallic **1** (A) and the TaCu congener **1$^{Cu}$** (B). Orbital isosurfaces are presented at a 0.04 eÅ$^{-3}$ level and energies, relative to the HOMO, are provided parenthetically.

## Table S2. Average Ta-arene Distances for Optimized Structures 1 - 4

| | Ring 1 | Ring 2 |
|---|---|---|
| **1** | 2.354 Å | 2.318 Å |
| **1$^{Cu}$** | 2.355 Å | 2.330 Å |
| **2** | 2.370 Å | 2.340 Å |
| **3** | 2.367 Å | 2.405 Å |
| **4** | 2.373 Å | 2.335 Å |

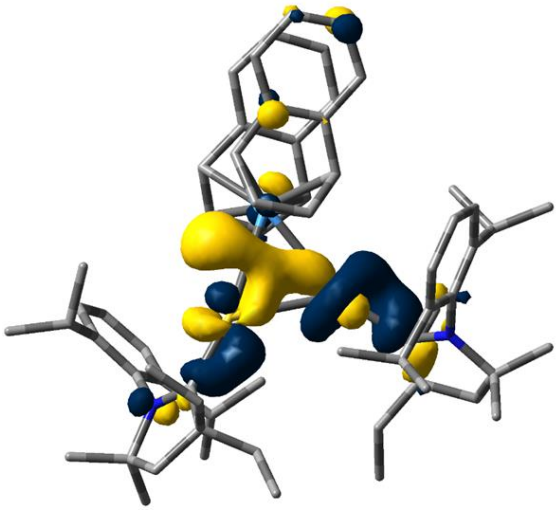

**Figure S36** – Select Kohn-Sham orbital (HOMO–7) for $TaAu_2$ trimetallic **2**, highlighting in-phase orbital overlap between the Au centers. The orbital isosurface is presented at a 0.04 $eÅ^{-3}$ level; hydrogen atoms are omitted from the structure for clarity.

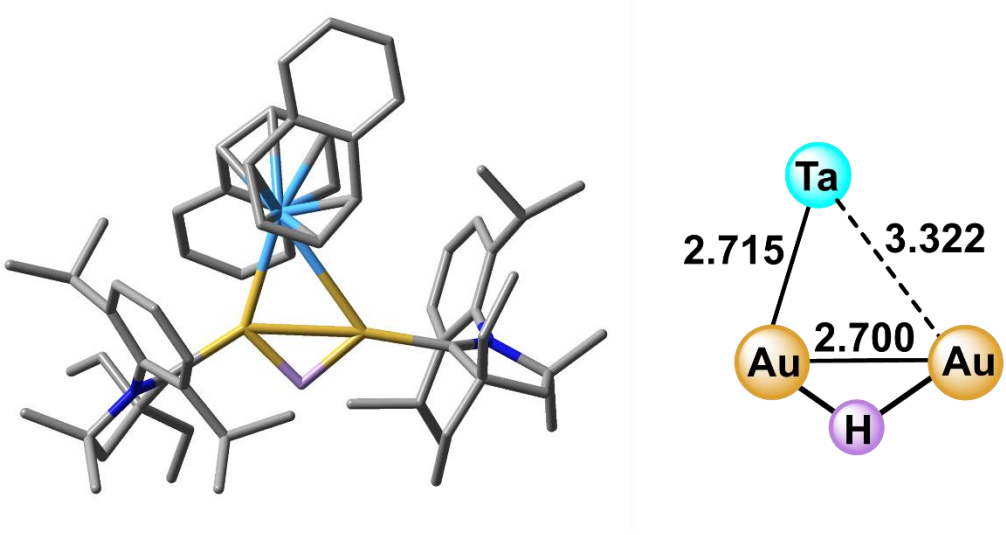


**Figure S37** – DFT optimized structure of **2'**, a structural isomer of **2** with the hydride located between the Au centers. Computed metrical parameters are provided for the truncated core, with bond distances reported in angstroms.

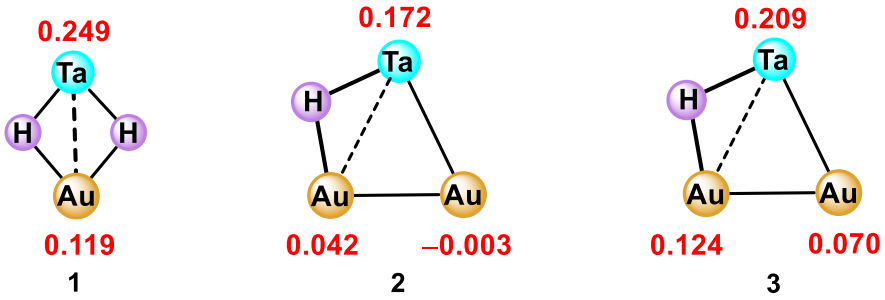


**Figure S38** – Hirshfeld charge analysis of complexes **1**, **2**, and **3** calculated at the same level of theory used for the optimization of each respective complex (see above).

## Additional Discussion of the Calculated Hirshfeld Charges:

To gain additional insight into the formal oxidation states in these clusters, we calculated Hirshfeld charges for species **1**, **2**, and **3**. These data show some clear trends. For instance, more oxidized clusters **1** and **3** showcase more positively charged metal ions. However, comparing the charges across the series, there is not a clear indication of a localized redox event at a particular metal center (or pair of metal centers) upon the two-electron oxidation of **2** (*ie.* both Au and the Ta center all increase in charge). For **1** and **3**, chemical intuition and the charges shown above, are consistent with Au(I) formal oxidation states. This would suggest a Ta(I) formal oxidation state in both clusters. However, this is less clear in **2**, where the Au centers may both be monocationic (net Ta(–I)Au(I)Au(I)) or where the unsupported Ta-bound Au may be Au(0) (net Ta(0)Au(I)Au(0); Hirschfeld charge = –0.003). We favor a Ta(–I) oxidation state, but this is not clear-cut in the Hirshfeld charge data. We likewise explored Ta-arene structural metrics as an experimental

indication of the formal oxidation state at Ta (see Tables S2 and S4); however, no significant metrical disparities were seen for any of the complexes in the series.

## *Crystallographic Information*

### Refinement Details

In each case, crystals were mounted on a MiTeGen loop, using Paratone oil, then placed on a Rigaku AFC10K Saturn 944+ CCD-based X-ray diffractometer equipped with a low temperature cryostream and a Mircomax-007HF Cu-target micro-focus rotating anode (λ = 1.54187 Å) operated at 1.2 kW power (40 kVm 30 mA). The X-ray intensities were measured at 85(1) K with the detector located at a distance of 42.00 mm from the crystal. Rigaku d*trek images were exported to CrysAlisPro[19] for processing and corrected for absorption using spherical harmonics, as implemented in the SCALE3 ABSPACK scaling algorithm.[20] Space groups were determined on the basis of systematic absences and intensity statistics and the structures were solved using SHELXTL intrinsic phasing (XT)[21] as incorporated into the Olex2 software interface.[22] Solutions were refined (SHELXL)[23] by full-matrix least squares on $F^2$ to convergence. All non-hydrogen atoms were refined using anisotropic displacement parameters and hydrogen atoms were placed in the idealized positions and refined using a riding model, unless noted otherwise. Graphical representations of structures with 50% probability thermal anisotropic displacement ellipsoids were generated as Posctscript vector images via Olex2.

**Table S3—Crystal and refinement data for complexes 1, 2, 4, 5, $2^{SIMes}$, and LAu(μH)AuL$^+$.**

| | 1 | 2 | 4 | 5 | $2^{SIMes}$ | LAu(μH)AuL$^+$ |
|---|---|---|---|---|---|---|
| CCDC Number[24] | 2409547 | 2409548 | 2409549 | 2409550 | 2432513 | 2432514 |
| Internal ID Code | mm359 | mm1142e | mm3155 | mm599 | mm141 | mm3171 |
| Empirical formula | $C_{46.13}H_{61.53}AuNO_{0.87}Ta$ | $C_{71}H_{93}Au_2N_2Ta$ | $C_{207}H_{234}Au_4B_2F_{48}N_4Ta_2$ | $C_{128.5}H_{146}Au_3BF_{24}N_3Ta$ | $C_{76}H_{85}Au_2N_4Ta$ | $C_{76}H_{82}Au_2BF_{24}N_2$ |
| Formula Weight | 1021.97 | 1549.35 | 4861.35 | 2971.13 | 1629.36 | 1884.17 |
| T (K) | 85 | 85 | 85 | 85 | 85 | 85 |
| *a*, Å | 17.1879(1) | 20.5343(2) | 19.5462 | 12.9225(1) | 11.30125(5) | 18.7780(2) |
| *b*, Å | 12.3223 | 13.9019(1) | 46.5001(2) | 23.8882(2) | 20.62174(10) | 22.0026(2) |
| *c*, Å | 39.3193 | 21.6795(2) | 21.9305(1) | 38.8158(3) | 28.44439(14) | 18.8760(2) |
| α, ° | 90 | 90 | 90 | 90 | 90 | 90 |
| β, ° | 96.0600 | 97.387(1) | 100.1400 | 94.395(1) | 96.4015(4) | 95.7150(10) |
| γ, ° | 90 | 90 | 90 | 90 | 90 | 90 |
| Volume, Å$^3$ | 8281.12(9) | 6137.39(9) | 19621.36(16) | 11947.02(17) | 6587.67(5) | 7760.13(14) |
| Z | 4 | 4 | 4 | 4 | 4 | 4 |
| Crystal system | Monoclinic | Monoclinic | Monoclinic | Monoclinic | Monoclinic | Monoclinic |
| Space group | $P2_1/c$ | $P2_1/n$ | $P2_1/n$ | $P2_1/c$ | $P2_1/c$ | $P2_1/n$ |
| $d_{calc}$, g/cm$^3$ | 1.666 | 1.677 | 1.597 | 1.575 | 1.643 | 1.613 |
| 2θ range, ° | 4.526 to 138.686 | 5.570 to 139.308 | 3.796 to 138.858 | 4.334 to 138.794 | 5.304 to 139.232 | 6.186 to 139.56 |
| $\mu$, mm$^{-1}$ | 11.609 | 12.324 | 8.300 | 9.121 | 11.529 | 7.888 |
| Abs. Correction | Multi-scan | Multi-scan | Multi-scan | Multi-scan | Multi-scan | Multi-scan |
| GOF | 1.059 | 1.068 | 1.072 | 1.110 | 1.177 | 1.613 |
| $R_1$,[a] $wR_2$ [b] [I>2 σ(I)] | 0.0288, 0.0744 | 0.0347, 0.0849 | 0.0477, 0.1245 | 0.0455, 0.1104 | 0.0337, 0.0925 | 0.0427, 0.1022 |
| Radiation Type | Cu Kα (λ = 1.54178) | Cu Kα (λ = 1.54178) | Cu Kα (λ = 1.54178) | Cu Kα (λ = 1.54178) | Cu Kα (λ = 1.54178) | Cu Kα (λ = 1.54178) |

[a] $R_1 = \sum||F_o| - |F_c||/\sum|F_o|$. [b] $wR_2 = [\sum[w(F_o^2-F_c^2)^2]/\sum[w(F_o^2)^2]]^{1/2}$

**Table S4—Average Ta-arene Distances for Complexes 1, $1^{Cu}$, 2, and 4 from SCXRD.**

| | $\eta^4$ | $\eta^6$ |
|---|---|---|
| **1** | 2.347 Å | 2.375 Å |
| **$1^{Cu}$** | 2.345 Å | 2.404 Å |
| **2** | 2.353 Å | 2.411 Å |
| **4** | 2.362 Å | 2.377 Å |

## Structure Determination of Complex 1

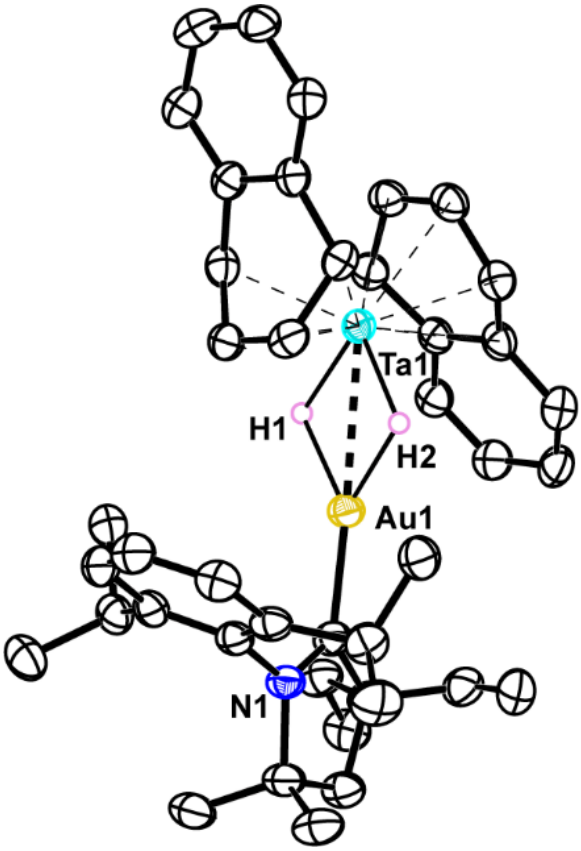


**Figure S39** – Structural drawing of **1** with 50% probability anisotropic displacement ellipsoids. There are two bimetallic complexes in the asymmetric unit. A representative molecule is shown above. The hydride hydrogens were discernable in the Fourier map; their locations were refined freely and their $U_{iso}$ values were treated with a riding model. Non-hydride hydrogen atoms are omitted for clarity.

**Special Refinement Details:** Disordered solvate molecules (THF and pentane) were present in the solid-state structure of **1**. One THF molecule (O1, C85 > C88) showed positional disorder of the oxygen atom which was satisfactorily modeled over two positions in a 50:50 ratio and refined with the O–$C_\alpha$ distances restrained to a target value of 1.427 Å. The other solvent void featured superimposed THF and n-pentane molecules. The O–$C_\alpha$ distances of each of these THF molecules (O2 C89 & C92 and O3 C93 & C96) were similarly restrained to a target value of 1.427 Å. Additionally, the $C_\beta$–$C_{\beta'}$ distances of all three THF molecules (C86 C87, C90 C91, and C94 C95, respectively) were tied together with 1,2-distance similarity restraints. The n-pentane moiety (C97 > C101) was refined with distance similarity restraints for the four C–C bonds. The superimposed THF/n-pentane occupancies were refined with a unity sum of their occupancies, and were further treated with both enhanced rigid bond and $U_{ij}$ restraints.

## Structure Determination of Complex 2

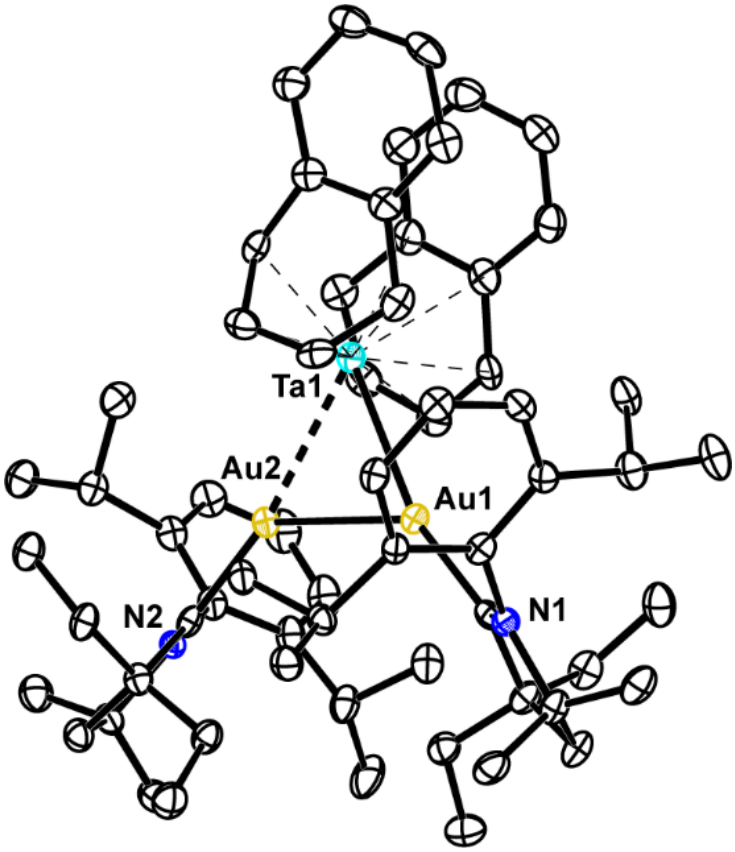


**Figure S40** – Structural drawing of **2** with 50% probability anisotropic displacement ellipsoids. Non-hydride hydrogen atoms are omitted for clarity.

**Special Refinement Details:** The hydride ligand was not discernable in the diffraction data for complex **2**. The reported empirical formula reflects the XRD data ($C_{71}H_{93}Au_2N_2Ta$); however, the accurate empirical formula for the complex includes an additional H-atom ($C_{71}H_{94}Au_2N_2Ta$)

## Structure Determination of Complex 4

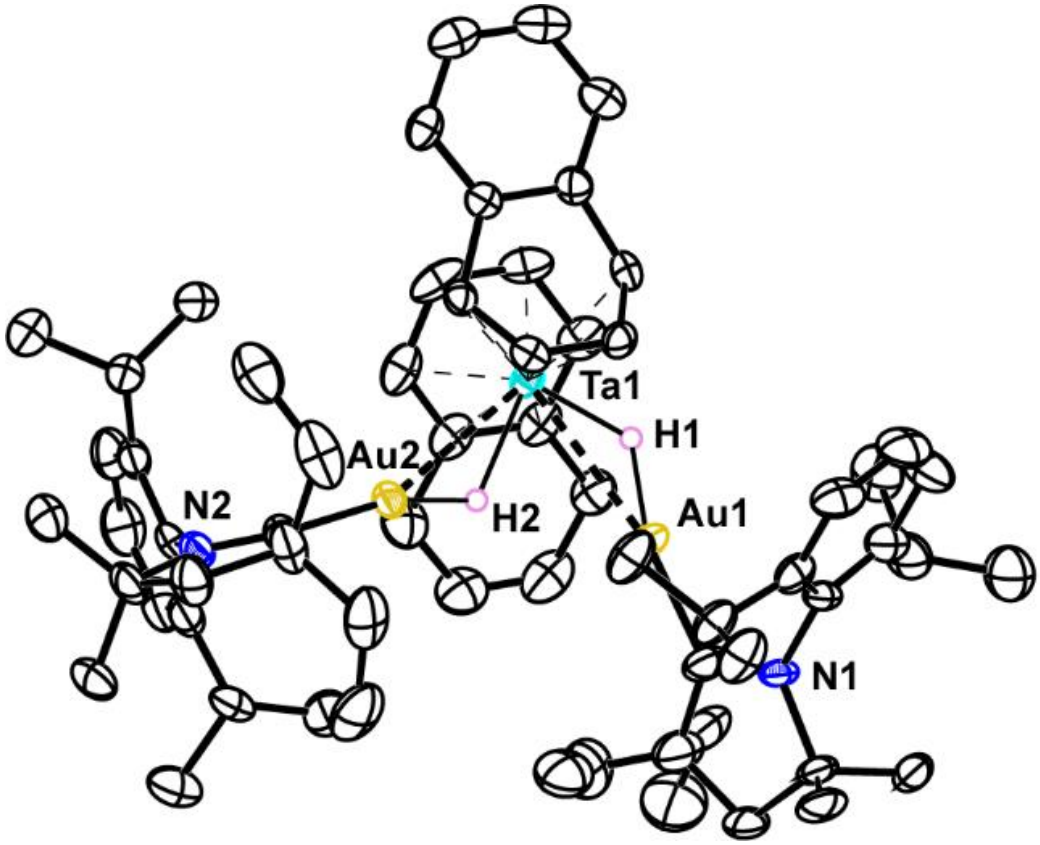


**Figure S41** – Structural drawing of **4** with 50% probability anisotropic displacement ellipsoids. There are two trimetallic complexes in the asymmetric unit. A representative molecule is shown above. The hydride hydrogens were discernable in the Fourier map; their locations were refined freely and their $U_{iso}$ values were treated with a riding model. Non-hydride hydrogen atoms are omitted for clarity.

**Special Refinement Details:** Crystals of **4** have a large unit cell (19621.36 $Å^3$), with two trimetallic moieties, two BArF counterions, and three pentane solvate molecules in the asymmetric unit. One of the primary residues (Ta1 Au1 Au2 H1 H2 N1 N2 C1 > C64) suffered from positional disorder of one of the CAAC ethyl groups. Given the low population of the minor component, modeling this disorder was unsuccessful, and instead, strong rigid bond restraints were applied to the motif (C21 C22 C23 C25 C26 C27). The remainder of the residue refined stably without restraints. The second primary residue (Ta2 Au3A/B Au4 H3 H4 N3 N4 C65 > C128) demonstrated significant positional disorder of one gold center and one of the two Ta-bound naphthyl rings. The former was satisfactorily modeled over two positions (in a 90:10 population ratio) with 1,2- and 1,3-distance similarity restraints. Despite best efforts, the disordered naphthyl ring could not be modeled satisfactorily over multiple positions and was instead restrained to have 1,2- and 1,3-distances akin to the comparable ring on the primary trimetallic residue. These distances were restrained with DFIX, rather than SAME, commands so that the bond metrics for the primary residue could be reported and were not affected by the positional disorder. Additionally, this Ta-$C_{10}H_8$ unit was treated with strong enhanced rigid bond and $U_{ij}$ similarity restraints.

As is common for BArF, both counterions suffered from rotational disorder of the $CF_3$ groups. In each case (C141 F4 > F6, C148 F7 > F9, C164 F19 > F21, C173 F28 > F30, C189 F40 > F42, and C196 F43 > F45) these groups were satisfactorily modeled over two positions with the use of 1,2- and 1,3-distance similarity restraints. Both counterions were refined with enhanced rigid bond restraints applied to the entire residue.

Finally, of the three pentane solvate molecules, only one could be refined freely. For the other two, a solvent mask was calculated and 368 electrons were found in a volume of 1732 $Å^3$ in five voids per unit cell. This is consistent with the presence of 2[$C_5H_{12}$] per formula unit which account for 336 electrons per unit cell.

Note: Complex **4** has two molecules in the asymmetric unit which both display unique positional disorders. Between the two molecules, there are a total of four Ta–Au bonds and only one has a minor disordered component (*ca.* 10%). This affords a strong set non-disordered data (three Ta–Au bonds) from which to extract meaningful (and reliable) metrical data.

## Structure Determination of Complex 5

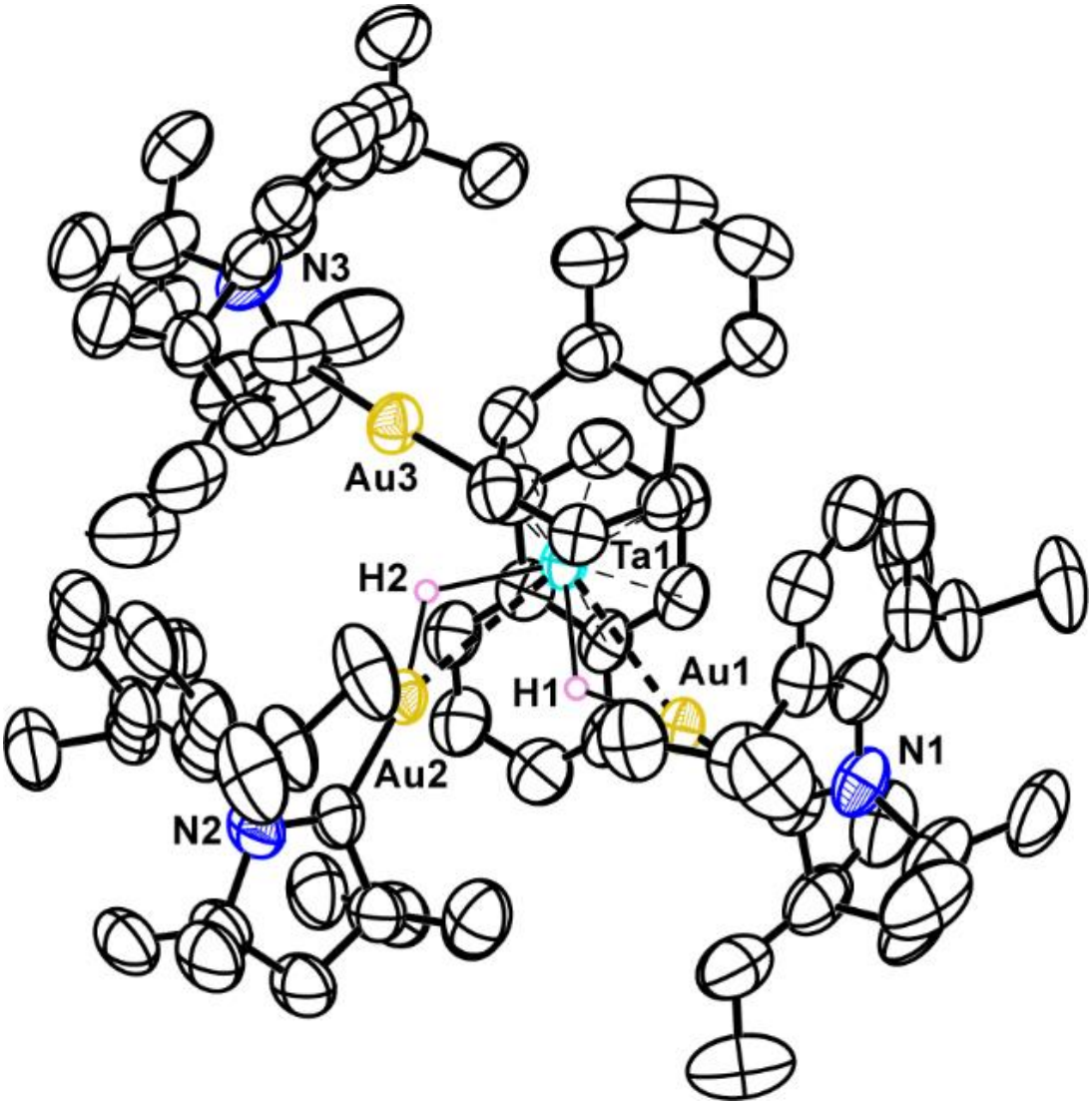


**Figure S42** – Structural drawing of **5** with 50% probability anisotropic displacement ellipsoids. Non-hydride hydrogen atoms are omitted for clarity. The hydride hydrogens were discernable in the Fourier map; their locations were refined freely and their $U_{iso}$ values were treated with a riding model.

**Special Refinement Details:** Crystals of **5** likewise grew with large unit cells (11947.02 Å$^3$), with one tetrametallic moieties, one BArF counterion, and toluene solvate molecules in the asymmetric unit. There was significant residual electron density in proximity to all four metal centers, which was treated as positional disordered. Each of the four metal centers was modeled over two positions (in a 66:33 population ratio), with the aid of 1,2- and 1,3-distance similarity restraints. All but one of the $CF_3$ groups on the BArF counterion suffered from rotational disorder (C93 F1 > F3, C94 F4 > F6, C102 F10 > F12, C109 F13 > F15, C110 F16 > F18, C117 F19 > F21, and C118 F22 > F24). These groups were satisfactorily modeled over two positions with the use of 1,2- and 1,3-distance similarity restraints. The counterion was refined with enhanced rigid bond restraints applied to the entire residue. Additionally, the toluene solvent models could not be modeled

discretely and were instead treated with a solvent mask. A solvent mask was calculated and 276 electrons were found in a volume of 1062 $Å^3$ in two voids per unit cell. This is consistent with the presence of 1.5[$C_7H_8$] per formula unit which account for 300 electrons per unit cell.

## Structure Determination of Complex $2^{SIMes}$

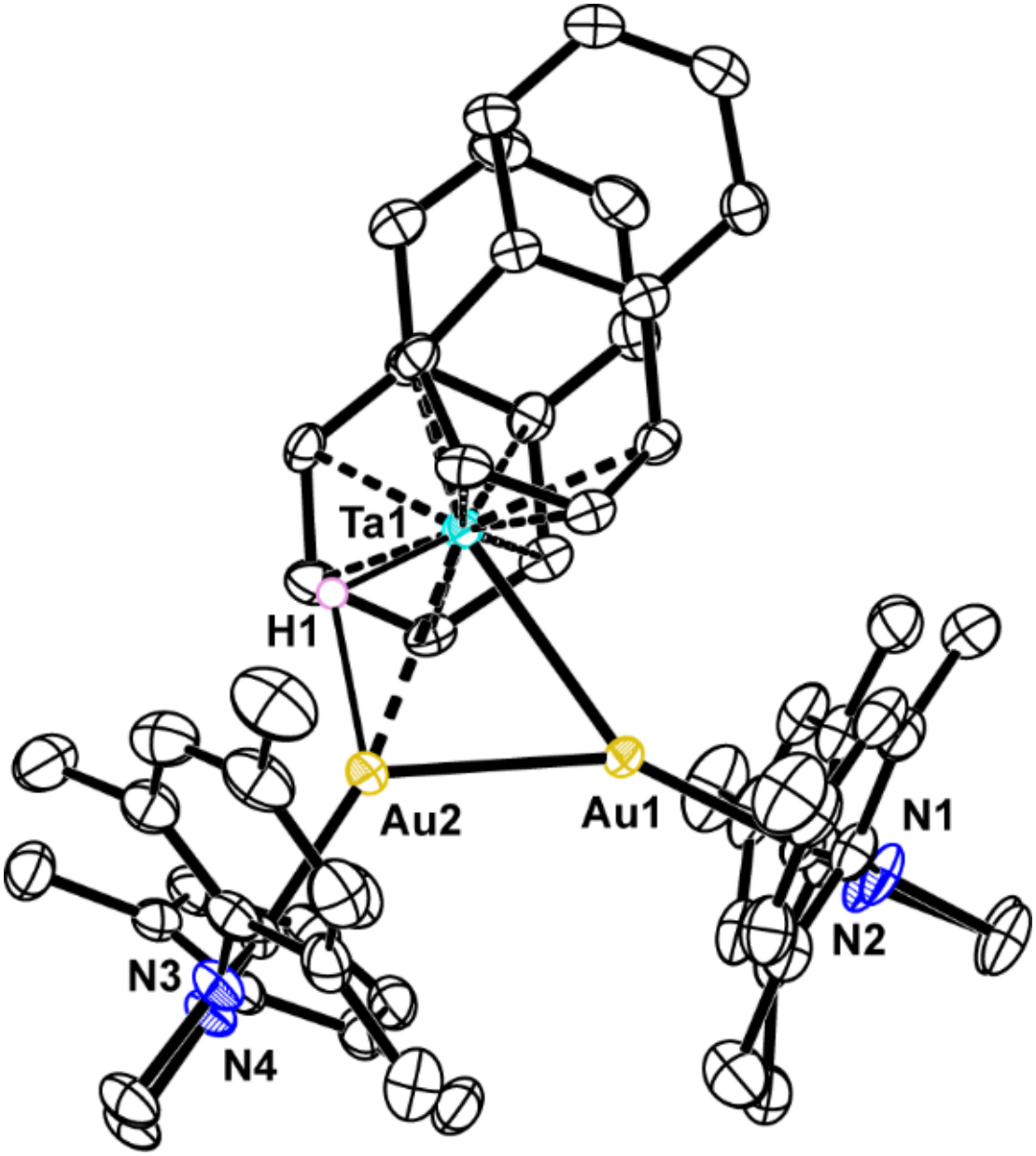


**Figure S43** – Structural drawing of $\mathbf{2}^{SIMes}$ with 50% probability anisotropic displacement ellipsoids. Non-hydride hydrogen atoms are omitted for clarity. The hydride hydrogens were discernable in the Fourier map; their locations were refined freely and their $U_{iso}$ values were treated with a riding model.

**Special Refinement Details:** Complex $\mathbf{2}^{SIMes}$ crystallizes with two toluene solvate molecules in the asymmetric unit. One of these solvates (C63 > C69) shows minimal positional disorder. The other was satisfactorily modeled over two discrete positions with a relative 66:44 population ratio. The components of this disorder (C70A > C75A & C70B > C75B) were restrained to have similar 1,2- and 1,3-distances and were refined with $U_{ij}$ and rigid bond restraints. The hydride ligand was discernable in the Fourier map, its position refined freely, and its $U_{iso}$ value treated with a riding model.

## Structure Determination of Complex LAu(μH)AuL$^+$

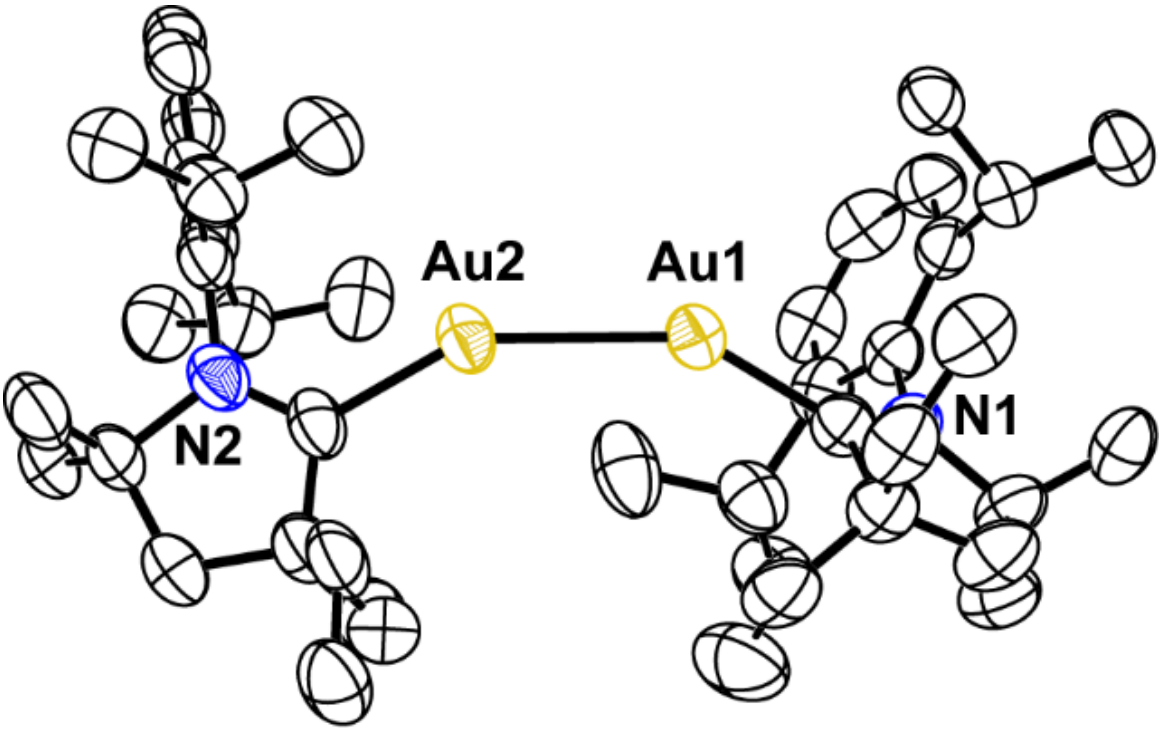


**Figure S44** – Structural drawing of LAu(μH)AuL$^+$ with 50% probability anisotropic displacement ellipsoids. Hydrogen atoms and counterions are omitted for clarity. The hydride hydrogen atom was not resolved in the Fourier map, however comparing the Au–Au bond distance (2.701 Å) and Au-Au-Carbene angles (150.85° and 148.73°) in this structure to a previously reported neutral LAu–AuL complex with a similar CAAC ligand (2.552 Å, 173.8°, 171.3°) we are confident this complex contains one bridging hydride ligand.[25]

**Special Refinement Details:** The main residue in this structure displays position disorder of three of the four CAAC ethyl arms (C21 C22, C41 C42, and C43 C44). In each case, this disorder was adequately modeled over two discrete positions with relative populations of 73:27 for each of the major and minor components, respectively. The C–C distances for each disordered group were restrained to be similar to that of the non-disordered ethyl moiety present in the structure (C19 C20). Furthermore, each disordered ethyl group was refined with $U_{ij}$ and rigid bond restraints.

There was significant positional disorder of the $CF_3$ groups in the BArF counterion. In two instances (C51 F1 > F3 & C60 F10 > F12), this disorder was best modeled as a two-component rotation of the $CF_3$ group about a shared C-atom. In the other three cases (C59 F7 > F9, C75 F19 > F21, C76 F22 > F24), the entire trifluoromethyl group was satisfactorily modeled over two positions. 1,2- and 1,3-distance similarity restraints were applied to all of the disordered groups and the entire residue was refined with $U_{ij}$ and rigid bond restraints.

The hydride ligand was not discernable in the diffraction data for **LAu(μH)AuL$^+$** (see note in Fig. S44 caption). The reported empirical formula reflects the XRD data ($C_{76}H_{82}Au_2BF_{24}N_2$); however, the accurate empirical formula for the complex includes an additional H-atom ($C_{76}H_{83}Au_2BF_{24}N_2$).

## *References*


[1] A. B. Pangborn, M. A. Giardello, R. H. Grubbs, R. K. Rosen, F. J. Timmers, *Organometallics* **1996**, *15*, 1518-1520.

[2] a) L. Zhou, D. Zhang, J. Hu, Y. Wu, J. Geng, X. Hu, *Organometallics* **2021**, *40*, 2643-2650; b) A. S. Romanov, C. R. Becker, C. E. James, D. Di, D. Credgington, M. Linnolahti, M. Bochmann, *Chem. Eur. J.* **2017**, *23*, 4625-4637.

[3] W. W. Brennessel, J. E. Ellis, M. K. Pomije, V. J. Sussman, E. Urnezius, V. G. Young, *J. Am. Chem. Soc.* **2002**, *124*, 10258-10259.

[4] M. Brookhart, B. Grant, A. F. Volpe, Jr., *Organometallics* **1992**, *11*, 3920-3922.

[5] I. Chávez, A. Alvarez-Carena, E. Molins*, A. Roig, W. Maniukiewicz, A. Arancibia, V. Arancibia, H. Brand, J. Manuel Manríquez*, *J. Organomet. Chem.* **2000**, *601*, 126-132.

[6] G. R. Fulmer, A. J. M. Miller, N. H. Sherden, H. E. Gottlieb, A. Nudelman, B. M. Stoltz, J. E. Bercaw, K. I. Goldberg, *Organometallics* **2010**, *29*, 2176-2179.

[7] a) P. T. Bell, W. L. Whaley, A. D. Tochterman, K. S. Mueller, L. D. Schultz, *J. Chem. Ed.* **2017**, *94*, 1969-1973; b) G. F. Pauli, S.-N. Chen, C. Simmler, D. C. Lankin, T. Gödecke, B. U. Jaki, J. B. Friesen, J. B. McAlpine, J. G. Napolitano, *J. Med. Chem.* **2014**, *57*, 9220-9231; c) G. K. Webster, S. Kumar, *Anal. Chem.* **2014**, *86*, 11474-11480; d) S. Mahajan, I. P. Singh, *Magn. Reson. Chem.* **2013**, *51*, 76-81; e) G. F. Pauli, T. Gödecke, B. U. Jaki, D. C. Lankin, *J. Nat. Prod.* **2012**, *75*, 834-851.

[8] R. E. H. Kuveke, L. Barwise, Y. van Ingen, K. Vashisth, N. Roberts, S. S. Chitnis, J. L. Dutton, C. D. Martin, R. L. Melen, *ACS Cent. Sci.* **2022**, *8*, 855-863.

[9] a) A. W. Beamer, J. A. Buss, *J. Am. Chem. Soc.* **2023**, *145*, 12911-12919; b) M. L. Maiola, J. A. Buss, *Angew. Chem. Int. Ed.* **2023**, *62*, e202311721.

[10] M. Landrini, R. Patel, J. Tyrrell-Thrower, A. Macchioni, D. L. Hughes, L. Tensi, P. Hrobárik, L. Rocchigiani, *Inorg. Chem.* **2024**, *63*, 13525-13545.

[11] M. J. Frisch, G. W. Trucks, H. B. Schlegel, G. E. Scuseria, M. A. Robb, J. R. Cheeseman, G. Scalmani, V. Barone, G. A. Petersson, H. Nakatsuji, X. Li, M. Caricato, A. V. Marenich, J. Bloino, B. G. Janesko, R. Gomperts, B. Mennucci, H. P. Hratchian, J. V. Ortiz, A. F. Izmaylov, J. L. Sonnenberg, Williams, F. Ding, F. Lipparini, F. Egidi, J. Goings, B. Peng, A. Petrone, T. Henderson, D. Ranasinghe, V. G. Zakrzewski, J. Gao, N. Rega, G. Zheng, W. Liang, M. Hada, M. Ehara, K. Toyota, R. Fukuda, J. Hasegawa, M. Ishida, T. Nakajima, Y. Honda, O. Kitao, H. Nakai, T. Vreven, K. Throssell, J. A. Montgomery Jr., J. E. Peralta, F. Ogliaro, M. J. Bearpark, J. J. Heyd, E. N. Brothers, K. N. Kudin, V. N. Staroverov, T. A. Keith, R. Kobayashi, J. Normand, K. Raghavachari, A. P. Rendell, J. C. Burant, S. S. Iyengar, J. Tomasi, M. Cossi, J. M. Millam, M. Klene, C. Adamo, R. Cammi, J. W. Ochterski, R. L. Martin, K. Morokuma, O. Farkas, J. B. Foresman, D. J. Fox, Wallingford, CT, **2016**.

[12] F. Weigend, R. Ahlrichs, *Phys. Chem. Chem. Phys.* **2005**, *7*, 3297-3305.

[13] D. Andrae, U. Häußermann, M. Dolg, H. Stoll, H. Preuß, *Theore. Chim. Acta* **1990**, *77*, 123-141.

[14] L. Rocchigiani, W. T. Klooster, S. J. Coles, D. L. Hughes, P. Hrobárik, M. Bochmann, *Chem. Eur. J.* **2020**, *26*, 8267-8280.

[15] S. Grimme, J. Antony, S. Ehrlich, H. Krieg, *J. Chem. Phys.* **2010**, *132*, 154104.

[16] F. L. Hirshfeld, *Theoret. Chim. Acta* **1977,** *44*, 129–138.

[17] T. Lu, F. Chen, *J. Comput. Chem.* **2012**, *33*, 580-592.

[18] Æ. Frisch, H. P. Hratchian, R. D. Dennington II, T. A. Keith, J. Millam, A. B. Nielsen, A. J. Holder and J. Hiscocks, *GaussView 5 Reference*, Gaussian, Inc., Wallingford, CT, **2009**.

[19] Agilent (2022). CrysAlis$^{Pro}$ Software System, version 1.171.42.61a. Agilent Technologies UK Ltd, Oxford, UK.

[20] SCALE3 ABSPACK - An Oxford Diffraction program (1.0.4,gui:1.0.3) (C) 2005 Oxford Diffraction Ltd.
[21] G. Sheldrick, *Acta Cryst. A* **2015**, *71*, 3-8.
[22] O. V. Dolomanov, L. J. Bourhis, R. J. Gildea, J. A. K. Howard, H. Puschmann, *J. Appl. Cryst.* **2009**, *42*, 339-341.
[23] G. Sheldrick, *Acta Cryst. C* **2015**, *71*, 3-8.
[24] Crystallographic data have been deposited at the CCDC, 12 Union Road, Cambridge CB2 1EZ, UK and copies can be otained on request, free of charge, by quoting the publication citation and the respective deposition numbers.
[25] D. S. Weinberger, M. Melaimi, C. E. Moore, A. L. Rheingold, G. Frenking, P. Jerabek, G. Bertrand, *Angew. Chem. Int. Ed.* **2013**, *52*, 8964-8967.